DESIGN AND ANALYSIS OF PHOTONIC STRUCTURES FOR SPECTRA DEPENDENT ENERGY HARVESTING OF PHOTOVOLTAIC DEVICES

A thesis submitted in partial fulfillment of the requirement for the degree

of

MASTER OF SCIENCE IN ELECTRICAL AND ELECTRONIC ENGINEERING

by

Ajanta Saha

STUDENT NUMBER: 1017062204 P

Department of Electrical and Electronic Engineering

Bangladesh University of Engineering and Technology

Dhaka-1000

December 11, 2019

Certification

The thesis titled "**DESIGN AND ANALYSIS OF PHOTONIC STRUCTURES FOR SPECTRA DEPENDENT ENERGY HARVESTING OF PHOTOVOLTAIC DEVICES**" submitted by Ajanta Saha, Student No.: 1017062204P, Session: October 2017, has been accepted as satisfactory in partial fulfillment of the requirement for the degree of MASTER OF SCIENCE IN ELECTRICAL AND ELECTRONIC ENGINEERING on December 11, 2019.

BOARD OF EXAMINERS

1. Dr. Md. Zunaid Baten
Assistant Professor
Department of Electrical and Electronic Engineering,
Bangladesh University of Engineering and Technology, Dhaka.
Chairman
(Supervisor)

2. Dr. Md. Shafiqul Islam
Professor and Head
Department of Electrical and Electronic Engineering,
Bangladesh University of Engineering and Technology, Dhaka.
Member
(Ex-officio)

3. Dr. Quazi Deen Mohd Khosru
Professor
Department of Electrical and Electronic Engineering,
Bangladesh University of Engineering and Technology, Dhaka.
Member

4. Dr. Sharif Mohammad Mominuzzaman
Professor
Department of Electrical and Electronic Engineering,
Bangladesh University of Engineering and Technology, Dhaka.
Member

5. Dr. Mohammed Abdul Basith
Professor
Department of Physics
Bangladesh University of Engineering and Technology, Dhaka
Member
(External)

Declaration

It is hereby declared that this thesis or any part of it has not been submitted elsewhere for the award of any degree or diploma and all sources are acknowledged.

Signature of the Candidate

Ajanta Saha

Ajanta Saha
(Student Number: 1017062204 P)

To my beloved parents….

Acknowledgement

First of all, I would like to thank Almighty for giving me the strength and perseverance to complete this thesis.

I would then like to express my sincere gratitude to my thesis supervisor, Dr. Md. Zunaid Baten, Assistant Professor, Department of Electrical and Electronic Engineering, BUET, for his constant support, thoughtful suggestions and encouragement throughout my thesis. I would also like to thank the other members of the thesis committee for taking the time to evaluate my work.

Last, but not the least, I would like to thank my family and friends for their support, encouragement and trust in my ability.

Abstract

In this thesis, we present a detailed study to design spectra selective photonic structures for harvesting energy efficiently from ambient light sources employing photovoltaic (PV) energy conversion technology. To choose the appropriate absorber material of the photonic structure, efficiency limit of single-junction PV devices for different absorber materials have been evaluated and optimum absorber bandgaps have been identified for natural and different artificial light sources. Due to widespread use of Red-Green-Blue (RGB) white LEDs, performance characteristics of ideal and practical PV devices have been studied in detail under white LED sources having a wide range of correlated color temperatures (CCTs) and fraction of blue in their corresponding spectrum and a relation has been established between maximum efficiency of the PV device and photometric features of the sources. Depending on bandgap of the absorber material, both positive and negative correlations are observed between photon conversion efficiency of PV devices and CCT values of the white LED sources. For material bandgaps of ~1.5eV or lower, higher photon conversion efficiencies are obtained for warm glow white LEDs. On the contrary, white LEDs characterized to emit cool light are found to be more conducive for PV devices having absorber layer bandgaps of ~2eV or higher. Upon selecting the absorber material we have designed the photonic structure having periodically arranged dielectric filled circular holes in the window layer of a practical PV device and evaluated optical absorption along with conversion efficiency of the device under solar irradiation and different white LEDs for a wide range of diameters and filling factors of the circular arrays. Based on the obtained results, a relation between optimum conversion efficiency of the PV device, filling factor of dielectric holes and photometric features of LED sources has been established. For absorber material bandgap of ~1.5eV, warm glow white LEDs outperform the cool light white LEDs and peak efficiency is obtained at relatively low filling factor (~40%) of dielectric holes. On the contrary, photonic structures with relatively high filling factor of holes (~70%) exhibit optimum conversion efficiency under white LEDs emitting cool light. Conversion efficiency of the photonic structures with filling factor in between 50% -70% is found to be optimum for operation under solar irradiation. These results in effect provide the necessary guidelines for designing homojunction, heterojunction or patterned PV devices suitable for operation under different light sources.

Table of Contents

List of Tables

List of Figures

Abbreviations of Technical Symbols and Terms

PV	Photovoltaic
LED	Light Emitting Diode
CFL	Compact Fluorescent Lamp
IOT	Internet of Thing
RGB	Red-Green-Blue
CCT	Correlated Color Temperature
CRI	Color Rendering Index
OSC	Organic Solar cell
DSC	Dye Solar cell
FDTD	Finite Difference Time Domain
ARC	Antireflection Coating
PP	Particle Plasmon
SPP	Surface-Plasmon Polaritons

CHAPTER 1
Introduction

Ambient light harvesting using photovoltaic (PV) devices has attracted great attention nowadays because of the unprecedented development of the Internet of Things (IOT). IOT promises a technological revolution where a wide variety of physical objects, such as consumer electronics, sensing nodes, household furniture, and personal belongings will be connected to the internet and be able to sense and interact with their internal states or the external environment. PV devices that harness energy efficiently from ambient light sources can be an alternative to conventional exhaustible sources of energy supply for the IOT components.

1.1 Literature Review

Energy harvesting by means of photovoltaic energy converters is considered to be the most promising among different techniques being employed for harnessing energy from renewable and non-exhaustible sources [1]–[3]. Research and development efforts in this area have primarily focused on scavenging solar energy by means of PV devices. However, with the advent of Internet of Things, there has been a growing demand for realizing ambient light based photovoltaic micro-energy harvesters which would be able to supplement, if not altogether replace, conventional exhaustible sources of energy supply for low-power electronic devices[4], [5]. The viability of harvesting ambient light by means of photovoltaic energy converters have been studied extensively over the recent years. Müller *et al.* [6] reported the optimal bandgap for typical narrow-band artificial light sources to be 1.9–2.0eV with 46% to 67% theoretical limiting efficiency of ideal photovoltaic converters. Along with theoretical studies, artificial light based photovoltaic devices capable of being integrated with IOT components have been designed and realized by many research groups. Thin film photovoltaic devices based on different material systems, such as silicon , GaAs, GaInP, CIS, CIGS , CZTSSe, CdTe , organics,

dye-sensitized materials and perovskites have been primarily used in these designs and implementations. Teran *et al.* [7] detemined the efficiencies of thin Si, GaAs and AlGaAs PV cells under typical white LED illumination and reported the highest power conversion efficiency of 21.1% for $Al_{0.2}Ga_{0.8}As$. Further Mathews *et al.*[8] implemented GaAs and GaInP- PV cells in credit-card-size and reported approximately ~4mW production of power under CFL or LED illumination (1000 lux). While record efficiency of CZTSSe based thin film PV device is 12.6% under sunlight, Haque *et al.* [9] designed a type II heterostructure that theoretically improves the efficiency to 15.85% under white LED. Besides, reserschers have also focused on effect of illuminating sources on PV devices perormance. Virtuani *et al.*[10] observed the performnace of $Cu(In,Ga)Se_2$ cell under fluorescent tube, halogen lamp and incandescent lamp and found strong influence of spectral distribution of the incoming light in the performance of $Cu(In,Ga)Se_2$. They reported that compared to performance of the cell under a AM 1.5 spectrum, power delivered by the cell to be reduced by a factor 3 and 2 respectively when using a fluorescent tube and a halogen lamp with cold reflector as the light source and to be increased by a factor 2.6 when operated under a halogen/incandescent lamp.

Flexibility of photovoltaic devices is highly desirable for seamless integration in IOT components. Águas et al. [6] replaced glass substrate of thin film amorphous Si solar cell with a suitable paper and achieved an efficiency of 3.4%, thus opened a door to flexible PV cells. Organic solar cells (OSCs) , dye solar cells (DSCs) and perovskite solar cells (PSCs) are strong candidates for such flexible PV cells. Lechêne et al. [13] achieved 7.6% power conversion efficiency under indoor conditions by optimizing the thickness of the electron transport layer of OSCs having an efficiency of 6.2% under sunlight. In a separate work, Goo et al. [7] recorded the maximum power-conversion efficiency of 13.9% for inverted OSCs using 8.5-nm-thick electron transport layer under LED light with a luminance of 500 lux. Rossi *et al.* [11] customized flexible dye solar cells by making electrolytes more transparent thus reached 12.4% efficiency under 200 lux CFL (more than quadruple compared to those measured at 1 sun) and 10% efficiency under 200 lux LED illumination. A strikingly high 28.9% power conversion efficiency was achieved under 1,000 lux indoor illumination by Freitag *et al.* [12] who introduced a new DSC design that combines two judiciously selected sensitizers and so enables incident

light to be harvested over the whole visible range. Lucarelli *et al.* [13] first proposed flexible planar and mesoscopic perovskite solar cell for artificial light harvesting that demonstrates an efficiency of 12.1% at 400 lux white LED lamp. Recently, Li *et al.* [14] reported a record indoor power conversion efficiency of 35.20% under fluorescent lamps of 1000 lux by interface modification of PSCs with ionic liquid.

One disadvantage of thin film photovoltaic devices is their low absorption of photons with energies close to that of the absorber layer's band-gap. For this reason, light trapping through photonic structures have steadily gained importance for thin film PV cells to increase the absorption without increasing the absorber thickness. Bozzola *et al.* [15] theoretically investigated the light-trapping properties of one- and two-dimensional periodic patterns etched on the front surface of c-Si and a-Si thin film solar cells and reported a substantial absorption enhancement, especially for 2D patterns and for thinner cells. Gomard *et al.* [16] practically implemented a 2D photonic structure having periodic circular air holes directly inside the amorphous silicon active layer and reported an increased absorption over the whole solar spectral range. They also suggested a global gain in cell efficiency by electro-optic simulations. Pratesi *et al.* [17] made similar studies for randomly structured thin film Si solar cell and reported strong absorption enhancement over the solar spectral range in fully random or weakly correlated photonic structures. Ishizaki et al. [18] reported an experimental efficiency of 8.7% in an ultra-thin (~500nm thick) microcrystalline Si solar cell, whose thickness is only 1/4 that of typical microcrystalline Si cells by incorporating photonic-crystal structures. There have been a large number of studies on size, position and configuration of photonic structures to obtain the optimum performance. Duch́ et al. [19] theoretically demonstrated a way of increasing absorption up to 35.6% in nanostructured OSCs by the coupling of slow Bloch modes in the squared matrix of P3HT nanowires embedded in PCBM. Mihi *et al.*[20]presented a theoretical analysis of the efficiency of dye sensitized solar cells in which colloidal crystals are introduced in different configurations. They found a maximum photocurrent enhancement of around 60% with respect to standard DSCs by piling up crystals of different lattice constants.

1.2 Motivation

Thin film PV devices which are able to operate efficiently under artificial low-light conditions, have been previously reported as promising power sources of IOT components [8], [9], [12], [21]–[24]. Illumination from different light sources, such as white LED, halogen lamp, incandescent lamp, sodium discharge lamp and fluorescent lamp have been considered in these studies [13], [25], [26]. However an aspect rather overlooked in such studies has been the detailed understanding of how performance characteristics of a PV device are influenced by the fine spectral features of the illuminating light source. The red-green-blue (RGB) white LED deserves particular attention in this regard because of the widespread commercial usage of these highly efficient and reliable light sources [27]–[29]. However it is yet to be reported how the choice of absorber material defines the energy conversion efficiency of a PV device when it is operated under white LED sources having different correlated color temperatures (CCTs) and fractions of blue in the emission spectrum. Moreover, in spite of extensive research on photonic structure design for solar cells [16], [17], [30], [31], there has not been any report on how photonic structures should be designed for photovoltaic devices operating under an artificial light source, such as a white LED source, the emission spectrum of which is significantly different from that of the solar spectrum. Therefore, it also remains to be seen how the design of the photonic structures should be tailored depending on spectral characteristics of different white LED sources.

1.3 Thesis Objective

The specific objectives of the thesis are the following:

I. To evaluate performance characteristics of PV devices operated under different artificial light sources and identify the optimum absorber material corresponding to the illuminating light source.

II. To establish the relation between maximum energy conversion efficiency of the PV device and photometric features of the white LED source.

III. To design spectra selective photonic structures which will be able to maximize conversion efficiency of the PV device when illuminated by the solar irradiation and different white LED sources.

1.4 Thesis Outline

Energy conversion efficiency of ideal PV converters having absorber layers of different material bandgaps has been evaluated employing detailed balance limit, taking into account illumination by different artificial light sources, such as incandescent lamp, white LEDs, fluorescent lamp and halogen lamp and optimal bandgaps of absorber material have been identified for the each of the sources. In order to evaluate performance characteristics of a practical thin-film PV device operated under commercially available RGB white LED sources, a theoretical model based on numerical solution of Poisson's equation and continuity equation has been employed. The obtained conversion efficiency of the PV device has been correlated with the white LEDs' photometric attributes, such as CCT, fraction of blue and emission linewidth. Next, in order to obtain a general framework, reference white LED spectra have been systematically generated such that they represent the wide range of color temperature of practical light sources. For these representative set of spectra, conversion efficiency of PV converters having different absorber materials have been evaluated and desired photometric features have been identified for maximum conversion efficiency of the considered PV device. In order to further enhance performance of the PV device, photonic structures comprising of dielectric filled holes in the active and window layers have been designed. Absorption characteristics of these structures have been computed by solving Maxwell's equation in three-dimension employing Finite Difference Time Domain (FDTD) technique. By varying diameters and filling factors/fractional area of the holes, light absorption and hence optical generation in the absorber layer have been enhanced to obtain optimal conversion efficiency of the device under consideration and the optimized photonic structure obtained for white LED illumination have been compared with that for solar irradiation to elucidate how the design of an optimum photonic structure is related to the spectral features of the illuminating light source.

The layout of the thesis is as follows. Chapter 2 presents key concepts of photovoltaic device for the characterization and numerical modeling of PV cells along with several photon management techniques to increase PV cells' optical absorption, hence power conversion efficiency. Chapter 3 explores structure modeling, computational details and methodologies. Chapter 4 contains the elaborate results and analysis of performance of PV devices of different absorber materials as well as PV devices incorporating photonic structures under natural and artificial sources. Finally, chapter 5 concludes the thesis with a brief discussion on possible future work in this direction.

CHAPTER 2
Theoretical Background

In this chapter key concepts for the characterization and numerical modeling of photovoltaic devices have been discussed. Moreover, several photon management techniques that are employed for enhancing optical absorption hence power conversion efficiency of the PV devices have been summarized. In the end, photometric features of solar and different artificial sources have been presented that are used as the illuminating sources of the PV devices.

2.1 Photovoltaic Technology Preliminaries

Photovoltaic effect is the creation of voltage and electric current in a material upon exposure to light. Light is made up of packets of energy, called photons, whose energy depends upon the frequency or color of the light. When light is absorbed by a material, photons are given up to excite electrons to higher energy states within the material. In a photovoltaic device, the built-in asymmetry pulls the excited electrons away and feeds them to an external circuit to do electrical work. The photovoltaic effect was first reported by Edmund Bequerel in 1839 and the first silicon photovoltaic cell was developed at Bell Laboratories in 1954 by Chapin et al. [32]. Since then photovoltaic cell technology has been emerged as a renewable energy source for its capability and long-term sustainability.

2.1.1 Photovoltaics for Renewable Energy

Photovoltaic cells have garnered a lot of attention due to the rising cost of fossil fuels and the increasing global demand for renewable sources of energy. Traditional photovoltaic research has been mostly focused on improving the efficiency and reducing the cost of photovoltaic cells. These efforts have brought about application of new materials and techniques in photovoltaic technology. Historically, there have been three generations of

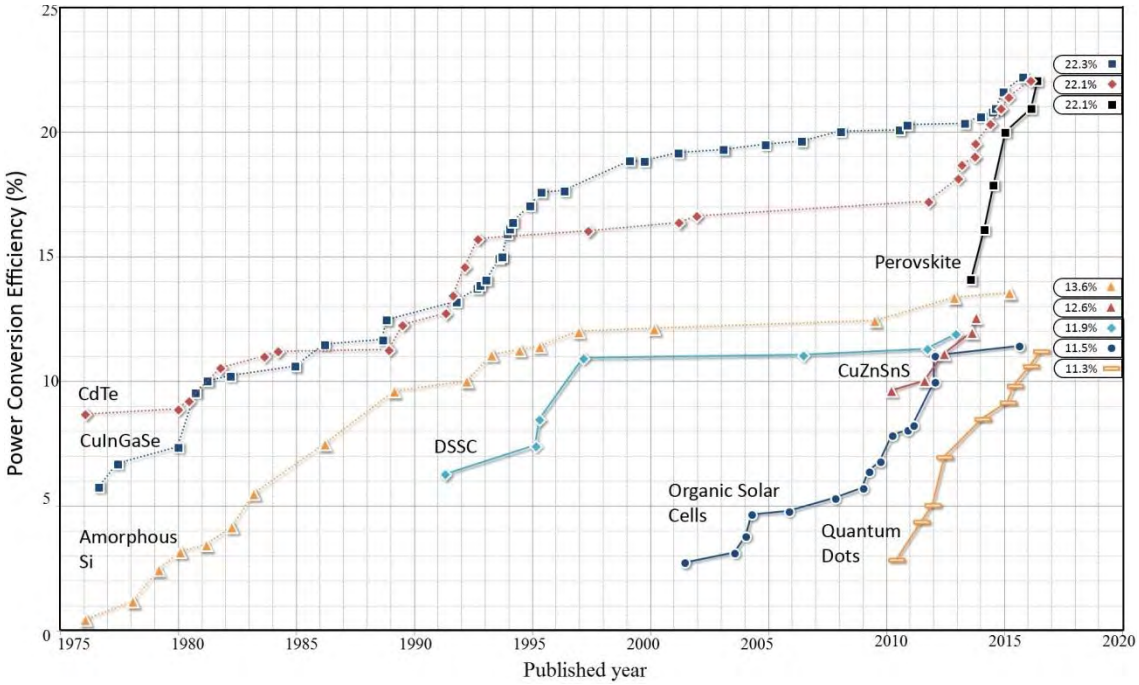

Figure 2.1 :PV cells power conversion efficiency over the years (adopted from [33])

photovoltaic technology [34]. The first generation represents the matured Si PV cell that was developed due to its availability and high power efficiencies. The second generation represents the thin-film technologies developed using low cost materials, such as copper indium gallium selenide (CIGS), cadmium telluride (CdTe), gallium arsenide (GaAs) and amorphous silicon (a-Si:H). The third generation represents advanced thin film technologies that use novel photovoltaic physics to go beyond traditional efficiency limits. This includes organic photovoltaics (OPVs), perovskite solar cells, dye-sensitised solar cells (DSSCs), and quantum dot solar cells [33]. Figure 2.1 demonstrates the achieved energy conversion efficiencies over the years for the three generations of photovoltaic technology.

In this technological era, cyber-physical systems are being the driving force of the fourth industrial revolution–that is defined by the ubiquity of emerging technologies. Internet of Thing devices and systems are at the forefront of these technological breakthroughs. Successful operation of cyber-physical systems largely relies on the fidelity of the constituent IOT components, which include wired or wireless communication nodes, sensors, actuators, microcontrollers and micro-chips [35], [36] . As the ratings of these

low-power electronic devices usually range between few micro-watts to several milliwatts, researches have been advanced in realizing new techniques of micro energy harvesting which would be able to supplement, if not altogether replace, exhaustible sources of energy supply for IOT and cyber-physical components [37]–[39]. Energy scavenging from ambient light sources in photovoltaic technique has attracted great attention in this respect primarily because of the maturity and proven track-record of the photovoltaic (PV) energy conversion technology[40], [41].

2.1.2 Physics of Photovoltaic Cell: Structure and Operation

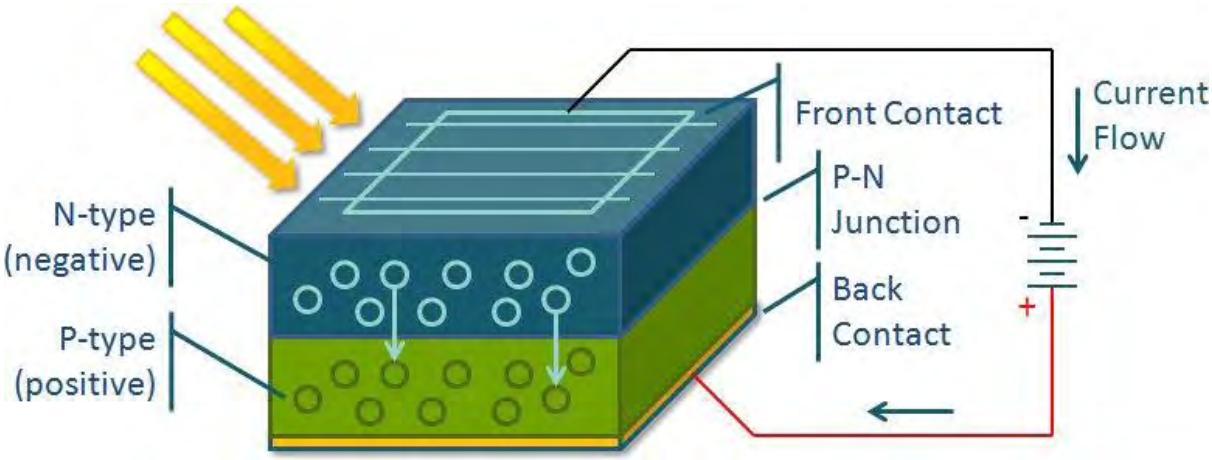

Figure 2.2 : Schematic illustration of photovoltaic device geometry

In the simplest possible structure of a photovoltaic cell, the active material (P-N junction) is sandwiched between two electrodes as shown in Figure 2.2. The active material absorbs energy from incident light on the material. If the energy of the incident photon (of light) is greater than the bandgap of the active material, electrons in the active material move from valence band to conduction band by absorbing the optical energy of the incident photon and free carriers are generated. The generated free carriers travel to the electrodes by drift (motion due to existing electric field in P-N junction) and diffusion (motion due to concentration gradient) mechanism. Upon reaching the electrodes, the free carriers contribute to current flow in the external circuit connected between electrodes.

Thus, electrical power is obtained if a load is attached in between the terminals of two electrodes. During their motion towards the electrodes, some carriers recombine with opposite carries and do not contribute in energy conversion. In short, the basic operation of a PV cell can be divided into:

1. Generation of free carriers
2. Transportation of free carriers towards respective electrodes
3. Collection of free carriers in the electrodes

2.1.3 Basic Characteristics of Photovoltaic Cell

The fundamental figures of merit for photovoltaic devices need to be understood in order to design them for optimal performance in a given environment. In the dark, diodes have a rectifying behavior which is described by the current density voltage relation,

$$J_{dark}(V) = J_0 \left[\exp\left(\frac{qV}{kT}\right) - 1\right] \tag{2.1}$$

where J_{dark} is the dark current density, J_0 is the dark saturation current density, q is the electron charge, V is the voltage across the cell terminals, k is Boltzmann's constant, and T is the temperature.

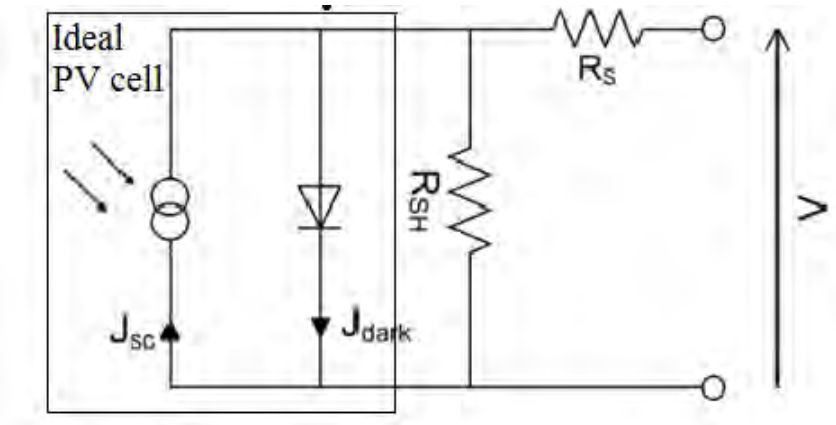

Figure 2.3 : Equivalent circuit of a photovoltaic cell

An ideal photovoltaic cell is electrically equivalent to a current generator in parallel with a diode as shown in Figure 2.3. When the photovoltaic cell is exposed to light, a photocurrent is generated which flows in the opposite direction of the dark current. The total current density in the photovoltaic cell is therefore,

$$J(V) = J_{SC} - J_{dark}(V) = J_{SC} - J_0\left[\exp\left(\frac{qV}{kT}\right) - 1\right] \tag{2.2}$$

Where J is the total current density and J_{SC} is the photocurrent density or short circuit current density which is proportional to the incident light's intensity. When the PV device is operated without load, the voltage across the output terminals is defined as the open-circuit voltage (V_{OC}). At V_{OC}, J_{SC} and J_{dark} cancel each other and Equation 2.2 equals zero. The resulting relationship demonstrates a logarithmic relationship between open-circuit voltage and light intensity given by,

$$V_{oc} = \frac{kT}{q} \times \ln\left(\frac{J_{SC}}{J_0} + 1\right) \tag{2.3}$$

The power density (P) of the photovoltaic cell is given by,

$$P = JV \tag{2.4}$$

Equation 2.4 has a maximum value (P_{max}) corresponding to the maximum power point of the photovoltaic cell. The fill factor of a photovoltaic cell is a ratio that gives significant information about its efficiency. Fill factor (FF) is defined as,

$$FF = \frac{P_{max}}{V_{OC}J_{SC}} \tag{2.5}$$

The power conversion efficiency of a photovoltaic cell can be defined using the relations defined above. If the incident light's power density is P_S, then the power conversion efficiency (η) is,

$$\eta = \frac{P_{max}}{P_S} = \frac{V_{OC}J_{SC}FF}{P_S} \tag{2.6}$$

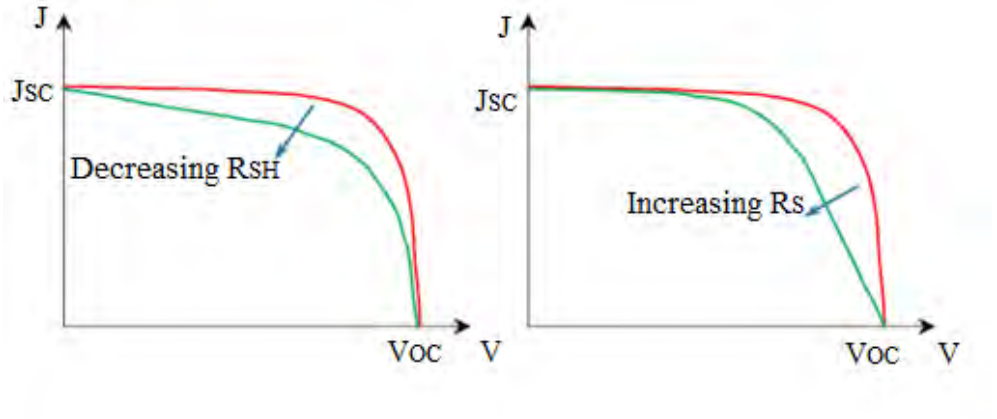

Figure 2.4 : Effect of changing R_{SH} & R_S from ideality

Practical PV devices can deviate substantially from the ideal PN junction PV cells due to a number of reasons. The photogenerated electron has to traverse a surface semiconductor region to reach the nearest electrode. All these electron paths introduce an effective series resistance R_s into the PV circuit as shown in Figure 2.3. A fraction of photogenerated carriers can also flow through the crystal surfaces (edges of the device) or through grain boundaries in polycrystalline devices instead of flowing through the external load. These effects are represented by an effective internal shunt or parallel resistance R_{SH}.

The series and shunt resistance can significantly deteriorate the PV cell performance. Decreasing R_{SH} and increasing R_s decrease the fill factor (FF) and P_{max} as illustrated in Figure 2.4. If R_{SH} is decreased too much, open circuit voltage (V_{OC}) will drop, while increasing R_S excessively can cause short circuit current (J_{SC}) to drop instead.

2.2 Modeling of Photovoltaic Cell

The common approach for numerical modeling of photovoltaic cells is based on the drift-diffusion formulation, where the Poisson equation is solved self- consistently with the current continuity equations under optical generation-recombination conditions for each layer of the heterostructure, taking into account relevant boundary conditions at the hetero-interfaces and at the top and bottom contacts of the device [42], [43]. The

generation of electron-hole pairs in this approach is determined by calculating the absorbed optical energy commonly by finite difference time domain (FDTD) model [44].

2.2.1 Finite Difference Time Domain Model

The FDTD approach is an approximate iterative solution method for Maxwell's curl equations in time domain. Maxwell's curl equations in non-magnetic materials are given by,

$$\frac{\partial \boldsymbol{H}}{\partial t} = -\frac{1}{\mu_o}\nabla \times \boldsymbol{E} \tag{2.7}$$

$$\frac{\partial \boldsymbol{D}}{\partial t} = \nabla \times \boldsymbol{H} \tag{2.8}$$

$$\boldsymbol{D} = \in_{\boldsymbol{0}} \in_{\boldsymbol{r}} (\omega)\boldsymbol{E}(\omega) \tag{2.9}$$

where $\boldsymbol{H}$, $\boldsymbol{E}$, and $\boldsymbol{D}$ are the magnetic, electric, and displacement fields respectively. The partial differential operators are discretized by using the finite difference expressions given by,

$$\frac{\boldsymbol{H}\left(t+\frac{\Delta t}{2}\right) - \boldsymbol{H}(t-\frac{\Delta t}{2})}{\Delta t} = -\frac{1}{\mu_o}\nabla \times \boldsymbol{E}(t) \tag{2.10}$$

$$\frac{\boldsymbol{E}(t+\Delta t) - \boldsymbol{E}(t)}{\Delta t} = \frac{1}{\epsilon}\nabla \times \boldsymbol{H}(t+\frac{\Delta t}{2}) \tag{2.11}$$

The discretized equations are solved in a leap-frog manner, that is the electric field intensity vector is solved at a given instant in time, followed by the calculation of the magnetic field intensity vector at the next instant in time. The workflow of solving Maxwell's equations is shown in Figure 2.5.

This method of solving Maxwell's equation was first proposed by Yee in 1966[45]. Yee proposed the leapfrog scheme for stepping in time such that electric field and magnetic field are temporally staggered. As a result, E-field updates are computed halfway of each

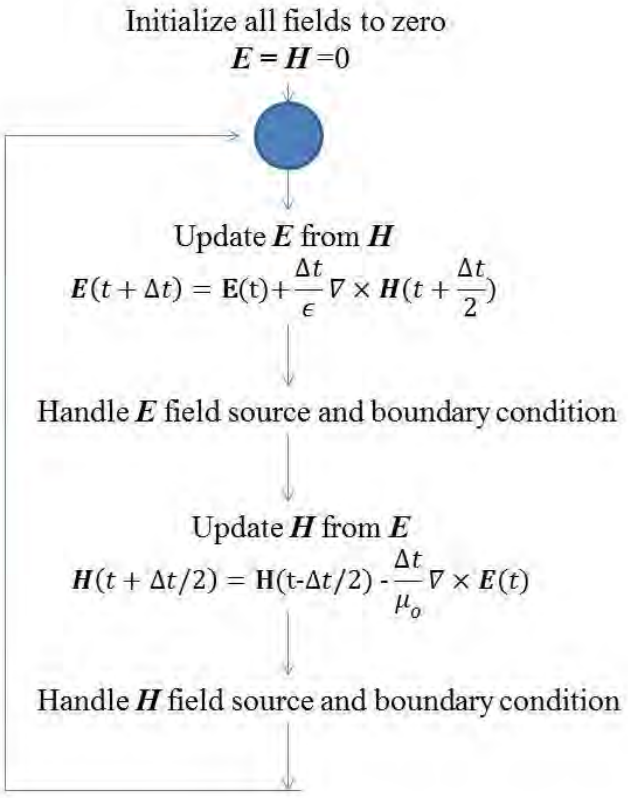

Figure 2.5: Work flow of Maxwell's equation solution

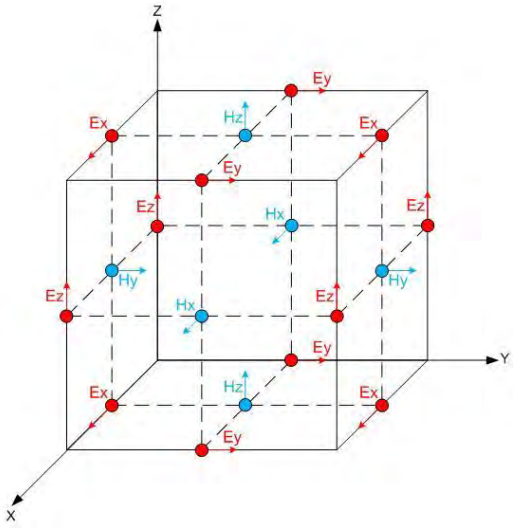

Figure 2.6: Yee grid in three-dimensional simulation domains(adopted from [45])

time-step between consecutive H-field updates and vice versa. Apart from proposing temporally staggered field vectors, a spatially staggered vector component of the E-field and H-field about rectangular unit cells of a Cartesian computational grid was proposed in this algorithm. It was arranged in a way so that each E-field vector component is located midway between a pair of H-field vector components. Figure 2.6 shows the arrangement of Yee grid for three-dimensional simulation regions.

For any arbitrary light source having input power P_{in} ,optical power absorbed per unit volume (P_{abs}) due to material absorption is determined from the above calculated E-field,

$$P_{abs} = -\frac{1}{2}\omega|\boldsymbol{E}(\boldsymbol{r},\omega)|^2 Im\{\epsilon(\boldsymbol{r},\omega)\} \tag{2.12}$$

Where ω is the angular frequency of incident light, $\boldsymbol{E}(\boldsymbol{r}, \omega)$ is the optical electric field distribution inside different layers of PV device and $\epsilon(\boldsymbol{r}, \omega)$ is the dielectric constant of the absorber material of each layer. Finally generation rate of the photo-generated electron-hole pairs $G(\boldsymbol{r})$ of the PV device illuminated by a light source with spectral power distribution $S(\omega)$ is obtained by,

$$G(\boldsymbol{r}) = \int g(\boldsymbol{r},\omega)d\omega \tag{2.13}$$

$$g(\boldsymbol{r},\omega) = \frac{S(\omega)}{P_{in}}\frac{P_{abs}}{\hbar\omega} = -\frac{S(\omega)}{P_{in}}\frac{\pi}{h}|\boldsymbol{E}\,(\boldsymbol{r},\omega)|^2 Im\,\{\epsilon\,(\boldsymbol{r},\omega)\} \tag{2.14}$$

2.2.2 Drift Diffusion Model

In Photovoltaic cell, the driving forces giving rise to current are electric field E and concentration gradients of electron (∇n) and hole (∇p). The drift current describes movement of charged particles, in this case electrons and holes in the presence of an electric field. The drift velocity of an electron is given by,

$$v_{drift} = -\mu E \tag{2.15}$$

where μ is the mobility which describes how well an electron or hole can move through the material. Now total drift current can be calculated by considering the total number of charged particles moving with drift velocity,

$$J_{drift} = -qnv_e + qpv_p = qE(n\mu_n + p\mu_p) = \sigma E \tag{2.16}$$

where n and p are electron and hole concentration respectively and σ is the conductivity of the material. Electric field can be expressed in terms of electric potential, as $E = -\nabla\psi$ Drift current is then given by,

$$J_{drift} = -q\nabla\psi(n\mu_n + p\mu_p) \tag{2.17}$$

Diffusion current arises when a gradient in the charge carrier concentration is present. Fick's law gives a relation between the electron diffusion current J_{diff}^{n} and ∇n .

$$J_{diff}^{n} = qD_n\nabla n \tag{2.18}$$

where D_n is the diffusion coefficient for electrons. A relation between diffusion coefficient and mobility is given by the Einstein relation,

$$D_{n,p} = \mu_{n,p}\frac{kT}{q} \tag{2.19}$$

Total diffusion current is obtained when including diffusion of both electrons and holes which is,

$$J_{diff} = q(D_n\nabla n - D_p\nabla p) = kT(\mu_n\nabla n - \mu_p\nabla p) \tag{2.20}$$

The total current for electrons and holes is given by the sum of drift and diffusion currents.

$$J_n = -qn\mu_n\nabla\psi + qD_n\nabla n \tag{2.21}$$

$$J_p = -qp\mu_p \nabla\psi - qD_p \nabla p$$

2.2.3 Poisson Equation Solver

To solve drift diffusion equations, potential variation in the semiconductor ($\nabla\psi$) has to be known which can be determined by solving Poisson's equation,

$$\nabla(\epsilon.\nabla\psi) = \rho = q(n - p + N_A^- - N_D^+) \tag{2.22}$$

where ε is the dielectric constant of the corresponding semiconductor, ρ is the total charge density, N_A^- is the ionized acceptor concentration and N_D^+ is the ionized donor concentration.

2.2.4 Continuity Equations

Finally the auxiliary continuity equations are required to account for charge conservation. The continuity equations describe the rate of change of free electrons and holes, thus relating the generation and recombination to the transport of charges. Continuity equations are given by the following expressions,

$$\frac{\partial n}{\partial t} = \frac{1}{q}\nabla . J_n + G_n - R_n$$
$$\frac{\partial p}{\partial t} = -\frac{1}{q}\nabla . J_p + G_p - R_p \tag{2.23}$$

At steady state time variant parts of (2.23) are zero. Here G_n and G_p are the electron and hole generation rates calculated from (2.13) and R_n and R_p are electron and hole recombination rates. Some important processes of recombination in PV cells are band to band recombination, Auger recombination and trap-assisted (Shockley-Read-Hall) recombination. In band to band recombination, electron and hole recombine in radiative manner and the recombination rate is,

$$R_B = r_{bb}(np - n_i^2) \tag{2.24}$$

here r_{bb} is band to band recombination coefficient. In trap assisted recombination one trapped and one free charge carrier recombine and its recombination rate is given by,

$$R_{SRH} = N_t C_n C_p \frac{np}{C_n(n + n_{th}) + C_p(p + p_{th})} \tag{2.25}$$

here N_t is the trap density, n_{th} and p_{th} is thermally excited electron and hole from conduction and valence band. In Auger recombination, two carriers recombine and the released energy is given to a third carrier which is excited to a higher energy level without moving to another energy band. Auger recombination rate for C_n and C_p are Auger capture probabilities is,

$$R_A = C_n n^2 p + C_p p^2 n \tag{2.26}$$

The system of equations consisting of Poisson's equation and the continuity equations can be solved in order to obtain the free charge carrier concentrations, potential and current density of the PV device.

2.3 Photon Management in Photovoltaic Cell

The aim of photon management is to enhance light absorption in the active layer of photovoltaic devices for achieving high-efficiency and cost-effective photovoltaic cells. The enhancement of light absorption is mainly performed in two ways: i) minimizing light reflection at the entrance and ii) confining light inside the active layers. Several photon management schemes based on nanostructures and nanotechnologies have already been proposed to attain these objectives. Different photon management strategies are useful in different conditions.

2.3.1 Reducing Reflection Loss by Antireflection Coating

One of the oldest techniques of increasing light absorption in photovoltaic cell is reducing reflection loss by antireflection coating. When light is incident on the surface of a semiconductor, a large portion of light is reflected due to mismatch of refractive indices between air and semiconductor. However, if the surface is coated with a thin dielectric layer of intermediate refractive index, reflected light intensity can be greatly reduced. This thin dielectric coating is known as antireflection coating (ARC) and the concept ARCs was conceived by Lord Rayleigh in the 19^{th} century [46]. After a long period of development, the most widely used ARCs in the industry are the quarter-wavelength-thick dielectric layers, due to their simplicity and cost and time effective fabrication processes. However, single quarter-wavelength ARCs only render the minimized reflectance at a narrow wavelength range and at nearly normal incident angles. To improve broadband and omnidirectional capability, double or multi-layered ARCs have been fabricated to suppress reflection over a wide range of wavelengths.

However, because of a lack of materials with refractive indices close to the refractive index of air, the AR performance is still not sufficient and to overcome these problems, nanostructures have begun to receive more attention[47] which provide an additional advantage by confining light in the PV devices.

2.3.2 Light Scattering by Textured Surfaces

Textured surfaces constitute an indispensable means to enhance the efficiency of thin-film PV cells by scattering the light into the active layer of the PV cell and suppressing reflection losses at the entrance facet as shown in Figure 2.7 [48]. In the early 1980s, Yablonovitch and Cody first derived the Lambertian limit of a light scattering scheme for the perfect scattering interface using statistical mechanics and geometrical optics approaches[49]. For a perfect scattering absorbing medium, the optical path length can be increased by a factor of $4n^2$ which means that the optical absorption can be enhanced by a factor of $4n^2$ compared to a flat surface.

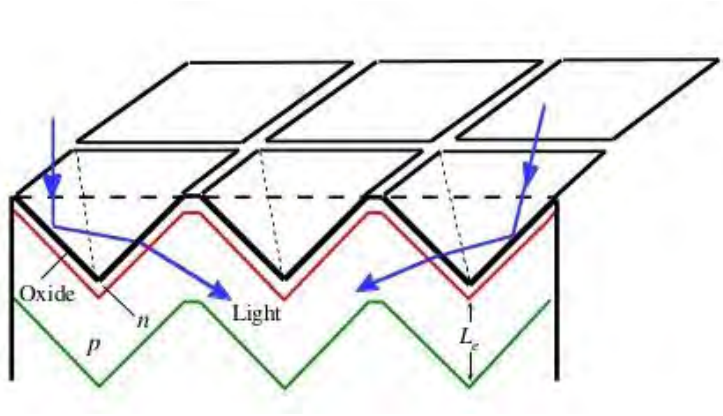

Figure 2.7: Light scattering by a systematic surface texture(adopted from [48] **)**

In thin film PV cells, the optimization of the surface profile is usually performed by experimentally modifying fabrication parameter and observing the effect on the absorption enhancement [48], [50]. The parameter in the focus of interest is usually the haze which is defined as,

$$Haze = \lim_{r\to\infty}\left[\frac{\int_0^2\int_0^{2\pi} S(r,\theta,\phi)d\theta d\phi - S(r,0,0)}{\int_0^2\int_0^{2\pi} S(r,\theta,\phi)d\theta d\phi}\right] \tag{2.27}$$

where θ and ϕ being the usual spherical coordinates and $S(r,\theta,\phi)$ being the radial component of the poynting vector $\boldsymbol{S}(r,\theta,\phi)$in the far-field. One limitation of light scattering structures is that the structures with large periodicity enhance absorption at long wavelengths by increasing the optical path length, but they are not beneficial for incident light transmission into the device.

2.3.3 Light Trapping with Diffraction Gratings

Diffraction gratings can be applied for light trapping in thin film PV cells to increase absorption of photons with energies close to that of the semiconductor's band-gap [51]. A grating is a periodic modulation of either an interface between two materials or of the permittivity itself. The periodicity can be along just one dimension or along two. The basic idea of this concept is sketched in Figure 2.8. Light incident on a grating (either at the front or at the rear side of a PV cell) is diffracted into a number of secondary beams of

different orders. The zeroth order corresponds to the direction of specular reflection which is the reflection that occurs without any grating. Light diffracted into higher orders travels along an oblique path and is totally internally reflected. The change of direction and the internal reflection provide the desired enhancement of the optical path length and absorption. How much light is trapped by a grating depends on its geometrical shape, its period, and the properties of the PV cell it is used for. Several research groups have investigated different grating geometries for optimizing gratings. Although most of the optimizations have been made for backside diffraction gratings[52], [53], combined front and back diffraction grating shows considerable promise in broadband enhanced absorption by ensuring absorption enhancement in a specific part of the light spectrum by each grating [54].

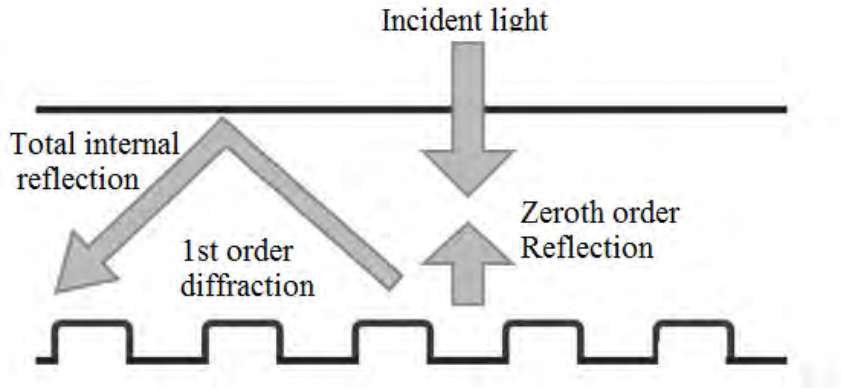

Figure 2.8: Principle of light trapping in a PV cell with a diffraction grating (adopted from [51]**).**

2.3.4 Light Confinement in Photonic Crystals

Photonic Crystals are natural or artificial materials which have a periodic arrangement of different dielectric materials in one, two or three dimensions as shown in Figure 2.9 [55]. The spatially arrangement hereby is in the range of the wavelength of the photon which is wished to be manipulated. The periodic arrangement affects the propagation of light in the same way as the periodic potential in a semiconductor crystal affects the electron motion. In photonic crystals, light is scattered at the interfaces where the index of refraction changes. The scattered waves can now interfere constructively or destructively

with each other. The stationary properties of the light that is allowed to travel are called modes. While the modes of propagation in a homogeneous medium are plane waves, the modes of a periodic medium are known as Bloch modes. Under certain conditions photonic band gaps can arise, which means that the formation of any mode is suppressed in the regarding energy range.

Photonic crystals can improve light confinement in two approaches. First, the energies of the photonic band gap, incident from any angle or medium are reflected back to the absorber layer. Second, a Bloch mode can be seen as a standing wave field produced by the multiple coherent scatterings of a wave by the periodic structures of a photonic crystal lattice. All of these effects can be thought of as increasing the time spent by photons inside the solar cell, which helps to maximize the probability of absorption [19], [31].

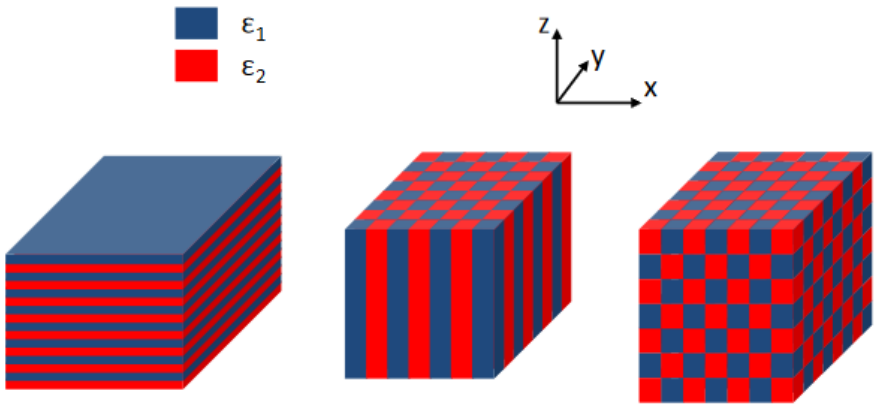

Figure 2.9: Layout of a one, two and three dimensional photonic crystal structure (adopted from [55])

2.3.5 Light Coupling by Plasmonic Structures

Another method for achieving light trapping in thin-film PV cells is the use of nanostructures made of metals such as silver and aluminum. The promising optical properties of metallic nanostructures are that they support surface plasmons which are excitations of the conduction electrons at the interface between a metal and a dielectric and are able to interact very strongly with the light field. In metal nanoparticles, they are

also called particle plasmons (PPs) or localized surface plasmons; on structured metal films, they are also known as surface-plasmon polaritons (SPPs) [56].

Plasmonic structures can reduce the physical thickness of the photovoltaic absorber layers while keeping their optical thickness constant in three ways[57]. First, metallic nanoparticles can be used as sub-wavelength scattering elements to couple and trap freely propagating plane waves from the source into an absorbing semiconductor thin film by folding the light into a thin absorber layer (Figure 2.10(a)). Second, metallic nanoparticles can be used as sub-wavelength antennas in which the plasmonic near-field is coupled to the semiconductor thus increasing its effective absorption cross-section (Figure 2.10(b)). Third, a corrugated metallic film on the back surface of a thin photovoltaic absorber layer can couple sunlight into SPP modes supported at the metal/semiconductor interface as well as guided modes in the semiconductor slab, whereupon the light is converted to photocarriers in the semiconductor (Figure 2.10(c)).

The major researches in plasmonic design include the choice of the metal, their shape and size, their dielectric environment and the electromagnetic coupling between them for tuning the plasmon excitations into spectral regions where they are the most useful for applications in PV cells [58], [59]. Appropriate resonance structure design strongly enhances light absorption under resonance conditions, but it is difficult to obtain broadband high absorption resonance.

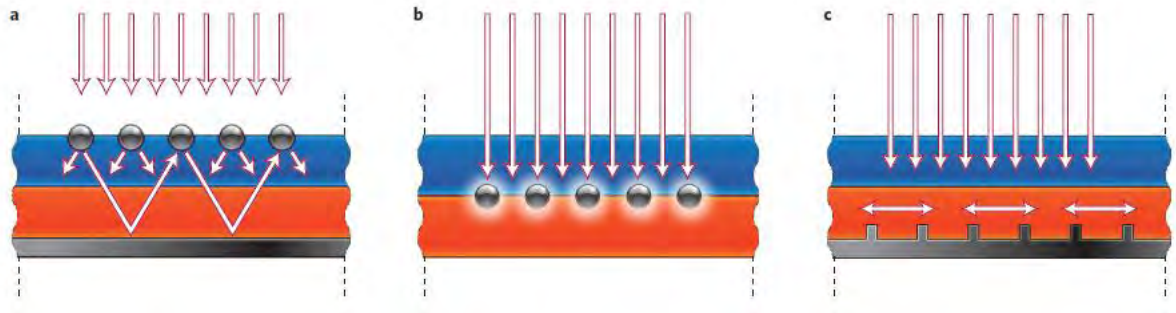

Figure 2.10 : Plasmonic light-trapping geometries for thin-film PV cells (adopted from [57])

2.4 Illuminating Source

Photovoltaic cell is an electrical device that converts the energy of light directly into electricity by the photovoltaic effect. The source of light is usually natural sunlight as most uses for photovoltaic devices are outdoors or in space. In addition to sunlight, artificial sources of light such as incandescent and fluorescent bulbs, RGB white LEDs can be potential sources of light for indoor photovoltaics.

2.4.1 Solar Irradiance

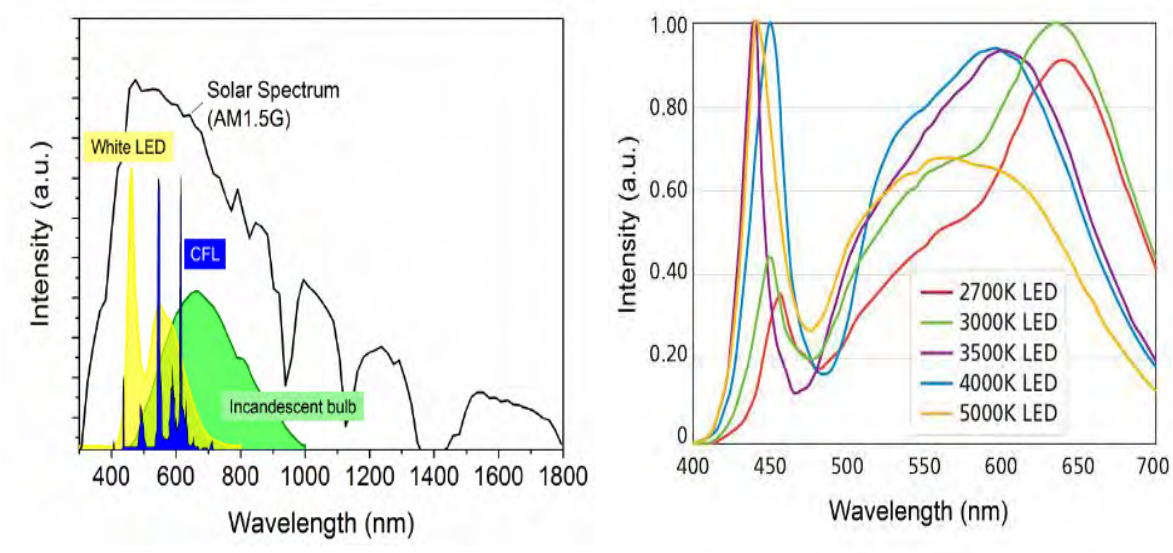

Figure 2.11 : Spectral Power Distribution of (a) artificial sources' compared to solar spectrum and (b) different commercially available White LED sources

The irradiance from a source of light is the amount of radiant energy received from the source per unit area per unit time. The solar spectrum contains light with a range of wavelengths that span from the high energy ultraviolet to the low energy infrared. The solar irradiance is the strongest in the visible range (400-700 nm) of the solar spectrum. This can be seen in Figure 2.11 which shows the solar irradiance at the surface of the earth as a function of wavelength. The solar spectrum can be approximated as the spectrum of a black body. A black body emits photon with a distribution of energies,

whose shape is determined by the characteristic temperature, T_S, of the black body. The T_S that best matches the solar spectrum is 5760 K. The spectral photon flux of a black body is given by,

$$b_s = \frac{2F_s}{h^3c^2}\frac{E^2}{\exp\left(\frac{E}{kT_s}\right) - 1} \tag{2.28}$$

where F_s is a geometrical factor which describes the angular range from the black body to the surface. This value is $2.16\text{x}10^{-5}\pi$ for the sun as seen from the earth. The irradiance of a black body is defined as

$$L(E) = Eb_s(E) \tag{2.29}$$

In order to determine the total power density emitted from a black body, (2.29) must be integrated over the full energy range of the spectrum. The total power density at the surface of the sun is 62 MWm^{-2}. This value is reduced to 1353 Wm^{-2} just outside the atmosphere of the earth. The earth's atmosphere reduces this value further because it filters parts of the spectrum. The total power density at the surface of the earth is around 900 Wm^{-2}. The standard solar spectrum that is used for determining figures of merit for photovoltaic devices is defined as the AM1.5 spectrum, whose integrated irradiance is 1000 Wm^{-2}.

2.4.2 Artificial Light Sources

In addition to solar irradiance, photovoltaic devices can be used to harvest energy from artificial light sources. As shown in figure 2.11(a) and (b), artificial light sources such as incandescent lamp, white LEDs, compact fluorescent lamp have a much narrower spectra compared with the solar spectrum since they were designed to be efficient light emitters in the visible region. The differences in spectrum shape among the light sources result in major differences in photovoltaic device performance and therefore design of PV devices should be different depending on the illuminating sources.

Artificial sources are typically characterized by color rendering index (CRI) and correlated color temperature (CCT). The CRI value of a light source describes how accurately a light source illuminates colors of an object and higher CRI values correspond to better color rendering. The highest possible CRI value is 100 that correspond to a source identical to standardized daylight or a black body. Incandescent lamp has a highest CRI due to a continuous spectrum similar to black body's emission. The discrete spectrum of fluorescent light is the cause of its low CRI of 50 and RGB White LED which is the most recent addition to artificial light sources, exhibits a CRI value of 75 to 95.

On the other hand, CCT is measured in Kelvin that helps to describe the relative warmth or coolness of a light source. Light sources with a CCT rating below 3200K are usually classified as "warm" and those with a CCT rating above 4000K are usually classified as "cool" in appearance. The effective range of CCT is 2000K-5500K for different types of artificial sources [60].

CHAPTER 3
Computational Methods

In the first section of this chapter, a semi-empiric model has been discussed to find the theoretical efficiency limits of ideal PV converters under solar spectrum and commercially available artificial sources. In the subsequent sections, structural details of practical PV devices have been presented and performance of the devices has been investigated under RGB white LED sources. Besides, a correlation between the PV device's performance and the illuminating source's photometric attributes has been established and a method has been proposed to generalize the findings for ideal PV converters of different material bandgaps. In the final sections of this chapter a systematic method to design a photonic structure has been discussed in order to further enhance the performance of PV devices under solar and white LED sources. We have first calculated optical absorption and then evaluated the energy conversion efficiencies of the photonic structures under consideration. Finally the design of the structure has been optimized to maximize conversion efficiency of the PV device when illuminated by the sources.

3.1 Theoretical Efficiency Limit

To choose appropriate absorbing material for the photonic structure under different lighting conditions, we have evaluated the Shockley-Queisser efficiency limit of an ideal PV converter for a wide range of absorber material bandgaps considering illumination from different light sources, such as solar irradiation, incandescent lamp, white LEDs, fluorescent lamp and halogen lamp [61].

Shockley-Queisser limits of the PV converters are calculated as per Green's approximation [6]. In this approach, for an ideal PV converter with an energy gap E_g irradiated by a spectral photon flux $\Phi(\lambda)$, photon yield (PY) is defined by,

$$PY = \int_0^{\lambda g} \Phi(\lambda)\, d\,\lambda \tag{3.1}$$

Where λg = hc/Eg, h is Planck's constant and c is the vacuum speed of light. In this approach, it is assumed that every photon with an energy E ≥ Eg creates a charge carrier, which is assumed to equal the elementary charge q = 1.601 × 10^{-19} C. In the ideal case, the short circuit current I_{sc} equals the photocurrent I_{ph} .

$$I_{sc} = I_{ph} = q \times PY \tag{3.2}$$

The dark current I_0 is calculated according to Shockley-Queisser formulation,

$$I_0 = qA\frac{2\pi k_B T}{h^3 c^2}(Eg + k_B T)^2 e^{-E_g/k_B T} \tag{3.3}$$

The area is denoted by *A*, Boltzmann's constant by k_B and the temperature by *T*. Open circuit voltage is calculated from,

$$V_{OC} = \frac{k_B T}{q} \times \ln(\frac{I_{ph}}{I_0} + 1) \tag{3.4}$$

Fill Factor is calculated from semiempirical approximation by Green with the normalized v_{OC}.

$$v_{OC} = \frac{V_{oc}}{k_B T/q} \tag{3.5}$$

$$FF = \frac{v_{OC} - \ln(v_{OC} + 0.72)}{1 + v_{OC}} \tag{3.6}$$

The maximum efficiency η depending on the input radiation power P_{in} is given by,

$$\eta = \frac{V_{oc} \times I_{sc} \times FF}{P_{in}} \tag{3.7}$$

It is quite obvious that theoretical efficiency limit will be different for different absorber material bandgap. However, for a particular absorber material the limiting efficiency also varies widely when operating under different illuminating sources. For a detailed understanding of how their performance characteristics are influenced by the fine spectral features of the illuminating light source a rigorous study is required. In our study, we have focused on red-green-blue (RGB) white LEDs because of the widespread commercial usage of these highly efficient and reliable light sources [62].

3.2 Practical PV Cell's Efficiency

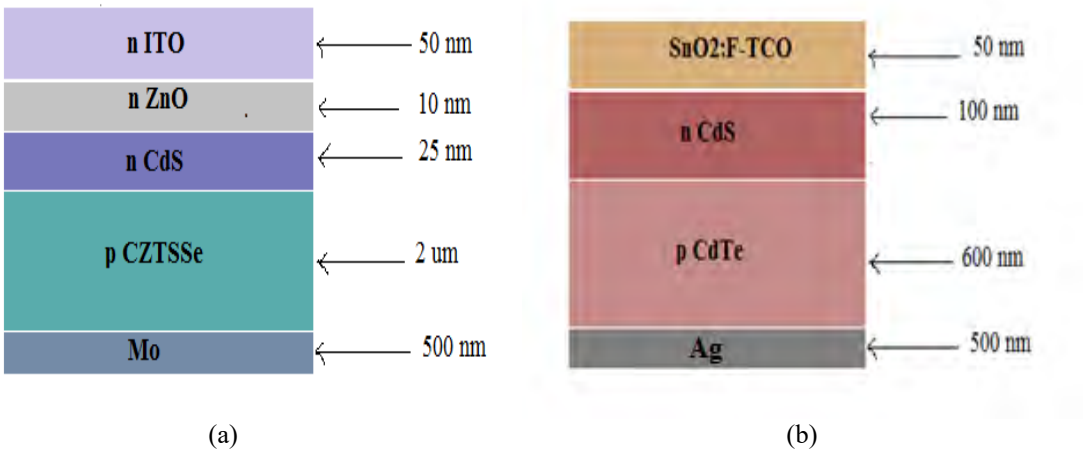

(a) (b)

Figure 3.1 : Cross section of simulated (a) CZTSSe device [63] **and (b) CdTe device**[64]

To investigate PV device's performance under white LED sources two different practical thin film devices have been considered. One is CZTSSe based which is a low cost renewable energy solution because of the abundance of its constituent elements in the earth [65]. Another one is CdTe based because of its superior performance as a thin film absorber material [66].

For the CZTSSe based PV device a 50 nm thick transparent conductive oxide Indium Tin Oxide (ITO) has been used as top contact and a 500 nm thick Molybdenum (Mo) layer as bottom contact. A 10nm thick Zinc Oxide (ZnO) layer and 25nm thick Cadmium Sulfide (CdS) layer are used as transparent buffer layer and window layer respectively. The active

Table 1: Values of material parameters used for the CZTSSe device in the study

Parameters	n-ZnO	n-CdS	p-CZTSSe
Layer thickness (cm)	$1x10^{-6}$[63]	$2.5x10^{-6}$[63]	$2x10^{-4}$[63]
Mobility gap (eV)	3.4[67]	2.34 [68]	1.13[69]
Optical gap (eV)	3.4	2.34	1.13
Donor doping (cm^{-3})	1×10^{16} [70]	1.5×10^{16} [71]	0
Acceptor doping (cm^{-3})	0	0	1×10^{16} [71]
Dielectric constant	7.96[67]	10 [68]	10 [69]
Electronic affinity (eV)	4.515[67]	4.9 [68]	4.422 [69]
Effective DOS in CB (cm^{-3})	3.92×10^{18}	2.22×10^{18}	4.22×10^{18}
Effective DOS in VB (cm^{-3})	3.34×10^{18}	1.8×10^{18}	4.2×10^{18}
Electron mobility ($cm^2V^{-1}s^{-1}$)	40 [72]	340 [72]	40 [73]
Hole mobility ($cm^2V^{-1}s^{-1}$)	3 [72]	100 [72]	10 [73]
Auger electron recombination coefficient (cm^6s^{-1})	0	5×10^{-10}[71]	3.5×10^{-22} [71]
Auger hole recombination coefficient (cm^6s^{-1})	0	0	1.5×10^{-26} [71]
Band to band recombination coefficient (cm^3s^{-1})	5×10^{-06} [71]	9×10^{-08} [71]	1×10^{-09} [71]
Series resistance ($ohm.cm^2$)	0.72[63]		
Shunt resistance ($ohm.cm^2$)	621[63]		

layer is 2 um thick Copper Zinc Tin Sulfide Selenite (CZTSSe) layer. The device structure is shown in figure. 3.1(a) and different material parameters used for the analysis of the device is listed in Table 1. For the CdTe device, a 50 nm thick Fluorine doped Tin Oxide (SnO_2: F) and 500 nm thick Silver (Ag) have been considered as top and bottom contact respectively. The window layer is 100 nm thick CdS layer and active layer is 0.6 um thick thin film Cadmium Telluride (CdTe) layer. Figure 3.1(b) shows the device structure and material parameters used for the analysis is listed in Table 2.

Table 2: Values of material parameters used for the CdTe device in the study

Parameters	n-CdS	p-CdTe
Layer thickness (cm)	$1x10^{-5}$[64]	$6x10^{-5}$[64]
Mobility gap (eV)	2.34 [68]	1.45 [74]
Optical gap (eV)	2.34	1.45
Donor doping (cm^{-3})	1 x 10^{17}[75]	0
Acceptor doping (cm^{-3})	0	2 x 10^{14}[75]
Dielectric constant	10 [68]	10.2 [76]
Electronic affinity (eV)	4.9[68]	4.52[76]
Effective DOS in CB (cm^{-3})	2.40 x 10^{18}	9.12 x 10^{17}
Effective DOS in VB (cm^{-3})	2.55x 10^{19}	1.66 x 10^{19}
Electron mobility ($cm^2V^{-1}s^{-1}$)	340 [72]	1050[74]
Hole mobility ($cm^2V^{-1}s^{-1}$)	100 [72]	100 [74]
Auger electron recombination coefficient (cm^6s^{-1})	1 x 10^{-34}[77]	1 x 10^{-34}[77]
Auger hole recombination coefficient (cm^6s^{-1})	1 x 10^{-34}	1x 10^{-34}
Band to band recombination coefficient (cm^3s^{-1})	1 x 10^{-6}[77]	1 x 10^{-6}[77]

Table 3: Comparison between I-V parameters of the experimental and simulated PV devices under AM1.5G solar spectrum

I-V parameters	CZTSSe device		CdTe device	
	Experimental values [63]	Simulated values	Experimental values[64]	Simulated Values
Short circuit current (mA/cm^2)	35.2	35.13	22.6	22.3
Open circuit voltage (V)	0.513	0.514	0.78	0.79
Fill factor (%)	69.8	69.9	63	66
Efficiency (%)	12.6	12.63	11.2	11.7

For the considered PV devices the generation rate of photogenerated electron hole pairs have been calculated in FDTD solver using (2.12) to (2.14). In (2.12), real and imaginary components of experimental dielectric constant for each material have been provided as inputs [78]. However, the experimental data cannot be used directly in the simulation. Instead, an analytic material model based on the experimental data is generated and used in the simulation. Periodic boundary condition has been used in planar direction to mimic infinitely large structures and perfectly matched layer (PML) boundary condition has been applied for top and bottom faces. Using the optical generation rate, the theoretical model based on numerical solution of Poisson's equation, drift–diffusion equation and continuity equation given in (2.15) to (2.23) is solved to find the conversion efficiencies of these practical PV devices under solar spectrum and the model has been validated based on the experimental results described in [63],[64]. A comparison between I-V parameters of the experimental and simulated PV devices are listed in Table 3. Finally energy conversion efficiencies of the devices have evaluated under different white LED sources.

3.3 Characterizing White LEDs

Correlated Color Temperature (CCT), a photometric attribute used to characterize light sources, represents the temperature of a black body in Kelvin that has the same chromaticity of the light source being analyzed. CCT of the white LED sources considered in this study are calculated as per the definition of CIE 1931 color spaces[79]. In this approach, the XYZ tristimulus values for each spectrum are calculated as per the following definition:

$$\begin{aligned} X &= K \sum_{\lambda=380}^{\lambda=780} S(\lambda) . \bar{x}(\lambda) \\ Y &= K \sum_{\lambda=380}^{\lambda=780} S(\lambda) . \bar{y}(\lambda) \\ Z &= K \sum_{\lambda=380}^{\lambda=780} S(\lambda) . \bar{z}(\lambda) \end{aligned} \tag{3.8}$$

Here, *S(λ)* is the spectral power distribution of the light source. $\tilde{x}(\lambda), \tilde{y}(\lambda)$ and $\tilde{z}(\lambda)$ are color matching functions shown in figure 3.2 and *K* is a normalization constant.

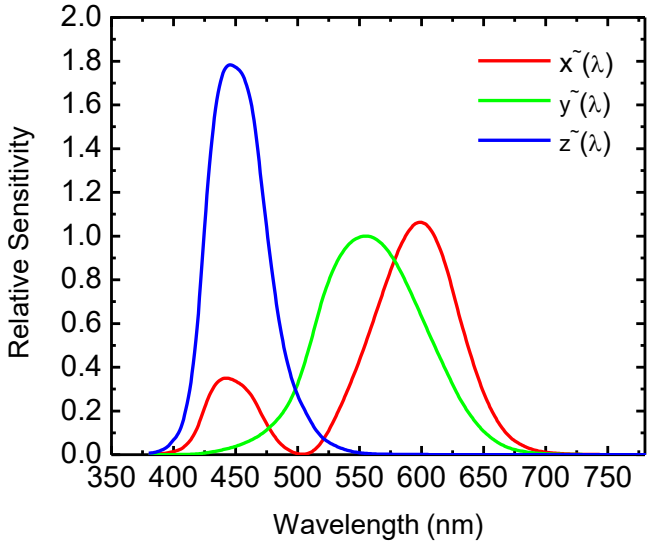

Figure 3.2 : Color matching function

The chromaticity coordinates (x, y) corresponding to the spectra are next obtained using (3.9):

$$x = \frac{X}{X+Y+Z}$$
$$y = \frac{X}{X+Y+Z} \qquad (3.9)$$

From these coordinates, the CCT values are finally estimated using McCamy's relation [80] defined as follows:

$$n = \frac{x - 0.3320}{0.1858 - y}$$

$$CCT = 449n^3 + 3525n^2 + 6823.3n + 5520.33 \qquad (3.10)$$

3.4 Correlating PV Cells' Efficiency with White LEDs' Photometric Features

The conversion efficiencies of the CZTSSe and CdTe based practical PV devices have been correlated with the CCT values of the illuminating white LED sources. Along with this, a correlation has been established between photon yield of the devices (assuming ideal PV converters) and CCT values to consider both ideal and practical cases.

In order to generalize the observed behavior of the PV converter under different white LED sources, reference spectra are systematically generated such that they cover the effective range of color temperature of typically available commercial white LEDs. It is important to note that CCT of a white LED source may vary depending on two factors, namely the variation of relative intensity of the blue emission peak (I_B) and the variation of linewidth ($\Delta\lambda$) of the broader emission centered at 600 nm. To account for both these factors, two different sets of LED spectra have been generated and considered. For the first sets of spectra, peak intensity of blue emission (I_B) is increased keeping $\Delta\lambda$ unchanged. The second sets of spectra are generated by varying $\Delta\lambda$ while keeping peak blue emission intensity constant.

To have an estimate of the fraction of light absorbed by an ideal PV converter under these spectra, photon yields are calculated for a wide range of absorbing material bandgap. Depending on the photon yield three characteristic bandgap regimes have been identified. Next photon yields are calculated for a particular material bandgap in each regime and a general relation has been established between photon yield and CCT in the regime. Thus we have established the relation between maximum energy conversion efficiency of the PV device of different absorbing materials and photometric features of the white LED source and evaluated maximum achievable efficiency of a PV converter under RGB white LEDs.

3.5 Optical Modeling of Photonic Structure

The photonic structure has been designed with the CdTe device shown in figure 3.1(b). The energy conversion efficiency of such ultrathin film PV devices (thickness <1um) is limited by poor absorption of a large fraction of the incident light [81], [82]. Light absorption hence optical generation has been increased by the optimized design of the photonic structure.

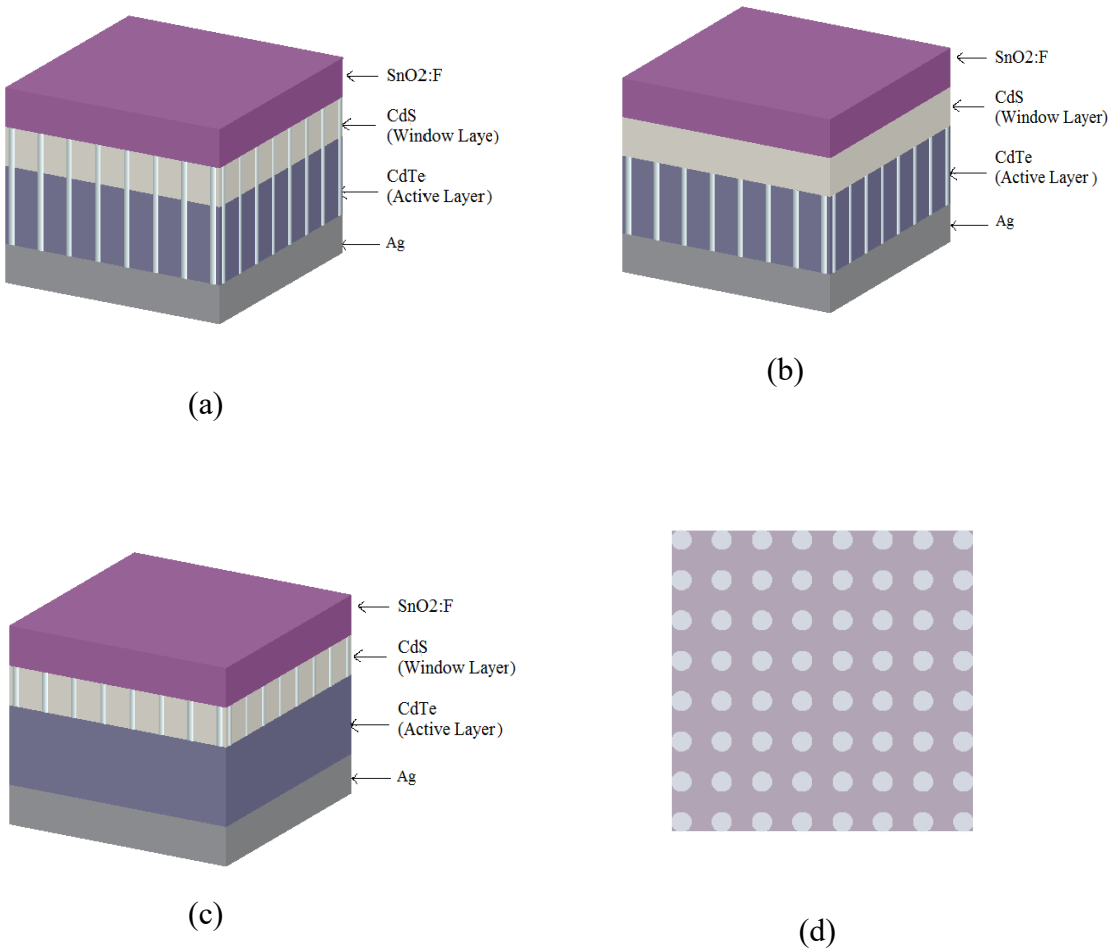

Figure 3.3 : Photonic structures with periodic SiO_2 holes in (a) both active and window layer (b) only active layer (c) only window layer and (d) top view of the structure

Three types of photonic structures made by patterning circular holes into active and window layer together, only active layer and only window layer have been considered in this study. The circular holes are arranged periodically and filled with dielectric material i.e. silicon dioxide (SiO_2). The structures are shown in figure 3.3.

In optical simulation, optical power absorbed by the whole photonic structure (P_{abs}) is calculated using (2.12) for a plane wave source and normalized by input source's power (P_{in}) to have fraction of incident power absorbed by the structure which is independent of any illuminating source. We have also observed fraction of power absorbed in active and window layer separately for the analysis purpose. Next generation rate of the photo-generated electron-hole pairs $G(\mathbf{r})$ of the patterned PV devices has been calculated for AM 1.5G standard solar spectrum and commercially available white LED sources using (2.13). Finally we have varied diameter and filling factor/fractional area ($FA=\pi r^2/a^2$, with radius of the holes r and lattice constant of the periodic holes a) of the circular arrays to enhance light absorption and hence optical generation in the absorber.

3.6 Electrical Modeling of Photonic Structure

The photogenerated carrier generation profiles obtained from the optical solver are inputs for the electrical modeling of the photonic structures. In the charge solver, short circuit current, open circuit voltage, fill factor and conversion efficiency of the photonic structures have been obtained under AM 1.5G standard solar spectrum and commercially available white LED sources by solving (2.15) to (2.23) using the generation profiles. Based on optimal conversion efficiencies under the sources, spectra selective photonic structures have been designed.

Material parameters used for the modeling are same as Table 2. However for the whole photonic structure, charge solver cannot solve the theoretical model based on Poisson's equation and continuity equation numerically. Therefore in numerical solution of the photonic structures, the effect of dielectric holes has been modeled by the resistance of the containing absorber layer. Since the dielectric filled holes are obstacles to the

transport of charges (electrons/holes) in the absorber material, the drift and diffusion current of the device will be reduced. The drift current density is given by:

$$J_{drift} = \sigma E \tag{3.11}$$

Where σ is the conductivity of the absorbing layer and E is the electric field. The reciprocal of the conductivity is resistivity ρ and the overall resistance of the layer with area A and length L is given by:

$$R = \frac{\rho L}{A} \tag{3.12}$$

$$\rho = \frac{1}{\sigma} \tag{3.13}$$

If the bare absorber layer has a resistance of R_{bare} and area of A_{bare}, after introducing dielectric filled holes effective area of the absorber layer will decrease to $A_{structure}$. Hence the effective resistance of the layer will increase to $R_{structure}$ according to the following relation,

$$\frac{R_{structure}}{R_{bare}} = \frac{A_{bare}}{A_{structure}} \tag{3.14}$$

Thus we have incorporated the effect of dielectric filled holes by making the absorbing layer containing the dielectric filled holes more resistive and increased the layer resistance in proportion to the reduced area. As a result, current density has been adjusted according to (3.11) to (3.13).

To evaluate the validity of our modeling, the effect of dielectric holes on photonic structure's output current density have been observed separately by including couple of holes in the absorber layer directly and by increasing layer resistances accordingly. We have numerically solved the actual and electrically modeled photonic structures in the charge solver and compared their performance under solar illumination.

CHAPTER 4
Results and Discussion

In this chapter, performance of ideal and practical PV devices has been presented for operation under natural and artificial light sources. Moreover, optical absorption and power conversion efficiencies of the considered photonic structures have been evaluated under solar and white LED sources. Based on the obtained results, spectra selective photonic structures have been designed which will be able to maximize conversion efficiency of the PV device when illuminated by the sources.

4.1 PV Device's Performance under Spectrally Varying Sources

In the first part of this section, energy conversion efficiencies of the ideal and our considered practical PV devices have been shown considering illumination under natural and commercially available artificial sources and optimum absorber materials have been identified for the corresponding light sources. In the subsequent part, performance of PV converters of different material bandgaps has been generalized based on operation under theoretically modeled white LED spectra. From these results a relation has been established between maximum energy conversion efficiency of the PV absorber material and photometric features of the white LED sources.

4.1.1 Characterization under Practical Light Sources

To evaluate performance characteristics of photovoltaic energy converters under typical lighting conditions, standard AM 1.5 solar spectrum and several commercially available artificial light sources have been considered in this study. Spectral power distribution ($S(\lambda)$) of these light sources are shown in Figure 4.1(a). In order to estimate maximum

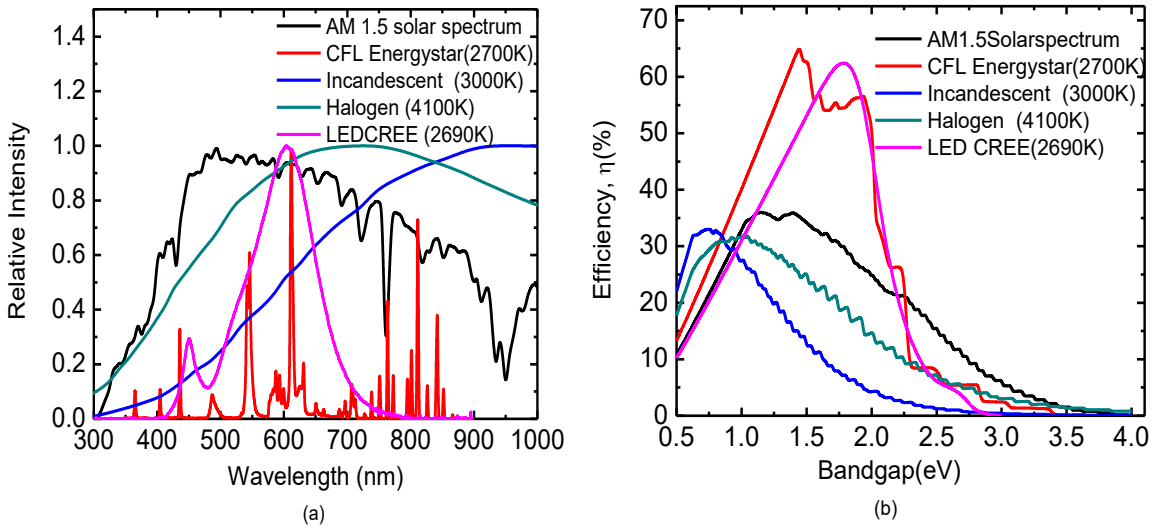

Figure 4.1 : (a) Spectral Power Distribution of AM 1.5 solar irradiation and artificial light sources (b) Limiting Shockley–Queisser efficiency of an ideal PV converter as a function of material bandgap under the illuminating sources.

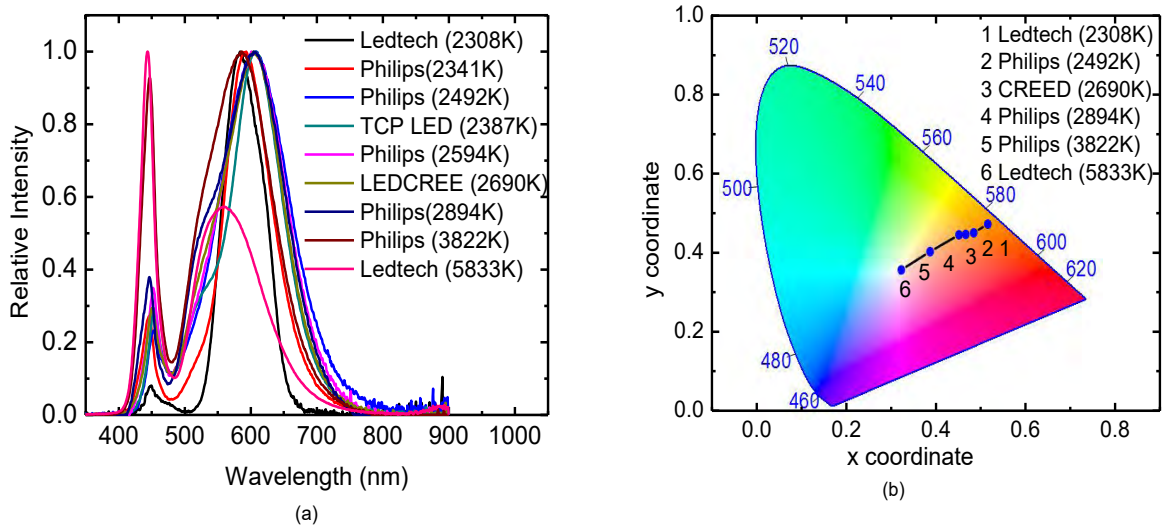

Figure 4.2 : (a) Spectral Power Distribution and (b) CIE 1931 Chromaticity diagram with chromaticity coordinates of commercial white LED sources (CCT values shown in parentheses)

conversion efficiency of an ideal PV converter under these practical light sources, Shockley-Queisser limits are calculated as per Green's approximation which is shown in Figure 4.1(b). The figure suggests that optimal bandgap energy of the PV absorber material varies depending on the illuminating source and for AM 1.5 solar irradiation, the

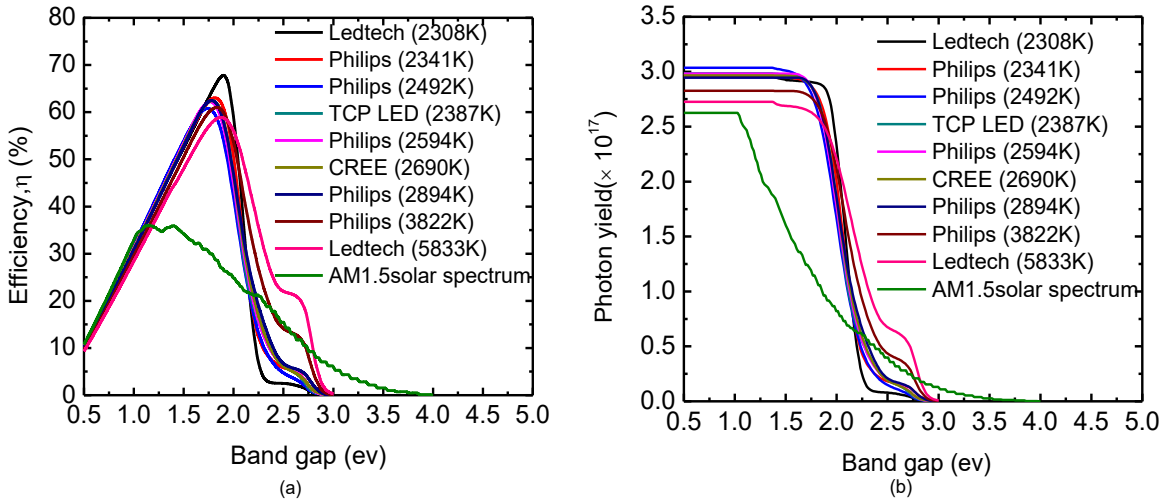

Figure 4.3: (a) Limiting Shockley–Queisser efficiency of an ideal PV converter as a function of material bandgap and (b) photon yield as a function of bandgap for different commercial white LED sources and AM 1.5 solar radiation.

limiting efficiency amounts to the range of 34% for absorber bandgap of 1.3eV whereas for Planckian radiators colder than the sun, the ideal maximum efficiency in our example decreases to 32% (incandescent bulb) and to 30% (halogen lamp) and peak efficiencies are recorded at bandgaps of 0.8eV and 1.0eV respectively for these sources. Among all artificial light sources, RGB white LEDs are highly efficient and mostly used now-a-days [83], [84]. So performance characteristics of PV devices have been further evaluated for fine spectral features of the RGB white LEDs. Figure 4.2(a) shows spectral power distribution (S(λ)) of some commercially available white LEDs having different correlated color temperatures, emission linewidths and relative intensity of blue. The CIE 1931 color space chromaticity diagram and calculated color temperatures for these spectra are depicted in Figure 4.2 (b). As can be seen, CCT values of the LEDs vary from 2308 K (warm glow) to 5833 K (cool white), which is basically the effective range of color temperature of typically available commercial white LEDs. In order to compare the performance of a PV converter under different white LEDs, Shockley-Queisser limiting efficiency is calculated for a wide range of absorbing material bandgap under the white LED sources and a comparative picture is shown in Figure 4.3 (a). As shown in Figure 4.3 (a), the peak efficiency limit for different bandgaps of the PV absorber material vary from 58%-68% over an optimal bandgap range of 1.7-1.9eV. These values are significantly higher than the maximum efficiency limit of 34% obtainable under AM1.5

solar irradiation. Such high values of efficiency limit can be explained in terms of the corresponding photon yields. The calculated photon yields for the white LED sources and also for AM1.5 solar spectrum are plotted in Figure 4.3 (b). It is to be noted that for the comparison of photon yield, intensity of each spectrum was scaled such that the total power density remains constant at 1000 W/m^2. As can be observed in Figure 4.3(b), for the entire range of bandgap, percentage of light absorbed by an ideal photovoltaic converter is much higher under a white LED source, than under solar radiation. It is also quite obvious that photon yield values obtained for different LEDs vary significantly depending on CCT of the illuminating spectra and bandgap of the PV absorber material, thereby indicating a possible correlation between the two.

To further investigate a PV device's performance under white LED sources having different CCTs, two practical PV converters, one CZTSSe-based and another CdTe-based thin film device is considered. The CZTSSe based device was previously reported to have demonstrated the record efficiency value of 12.6% under solar irradiation [85] and a theoretical efficiency value of 13.77% under typical white LED illumination [9]. Although maximum efficiency of CdTe based device has already been obtained to 22.1% under solar irradiation [86] ,our considered device exhibits an experimental efficiency of

Table 4: LED sources with their CCTs and corresponding efficiencies of the CZTSSe and CdTe device

White LED source	CCT of the LED (K)	Efficiency of the CZTSSe device (%)	Efficiency of the CdTe device (%)
Ledtech Bridgelux	2308	14.61	18.71
Philips Streetview	2341	14.77	18.92
TCP LED PAR20	2387	14.8	18.86
Philips LED A19	2492	14.98	19.02
Philips LED CandleLight	2594	14.81	18.93
CREE LED BR30	2690	14.8	18.85
Philips LED PAR20 Flood	2894	14.68	18.74
Philips LED 3white-board	3822	14.14	17.83
Ledtech LED PAR20	5833	13.55	16.73

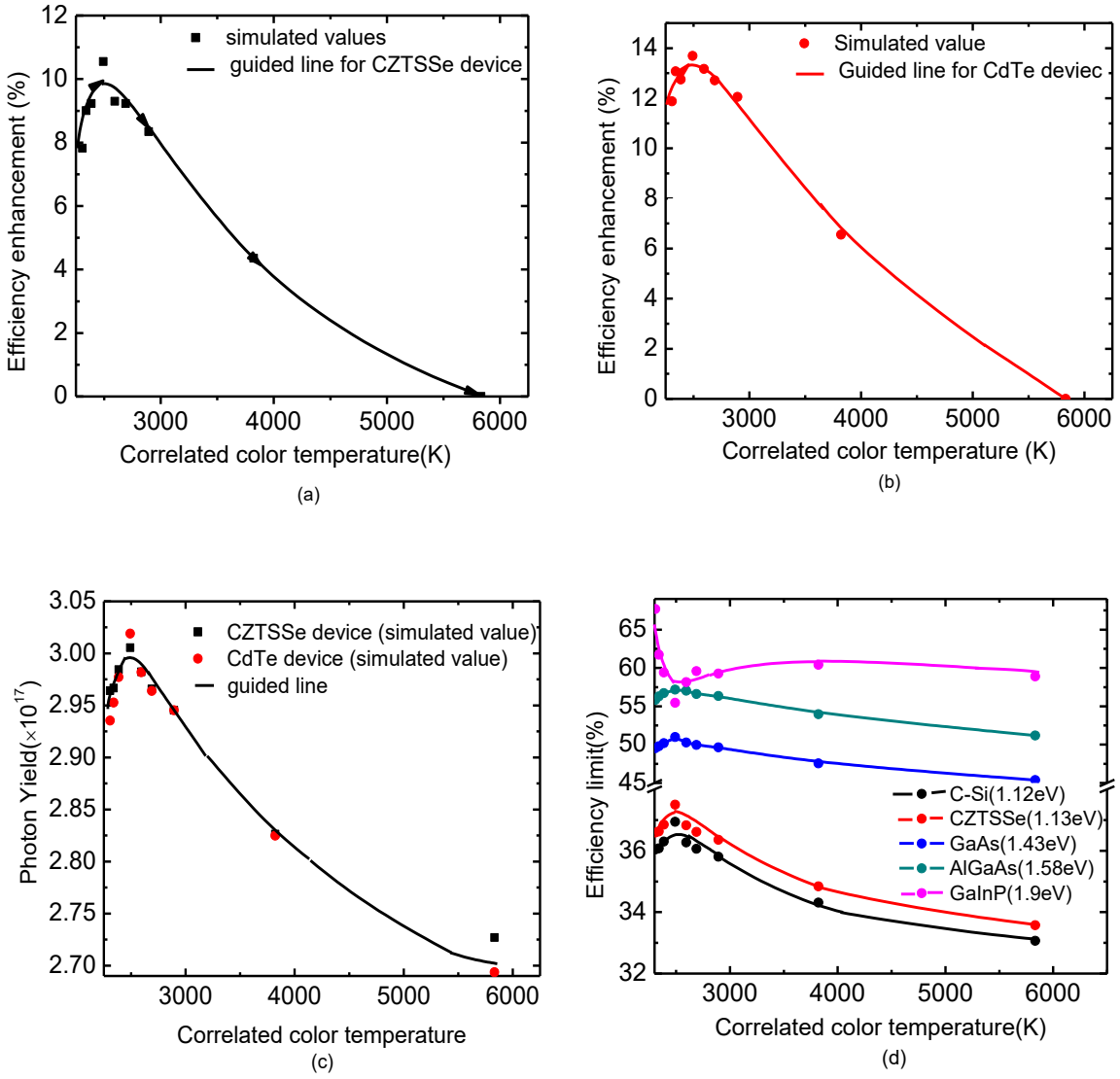

Figure 4.4: Relative enhancement of efficiency taking the lowest efficiency as reference for (a) CZTSSe and (b) CdTe device (c) calculated photon yield as a function of CCT of the commercial LED sources for the CZTSSe and CdTe device and (d) limiting Shockley–Queisser efficiency of an ideal PV converter of different absorber materials (bandgaps shown in parentheses) as a function of CCT of the commercial LED sources

11.2% which is maximum recorded efficiency for CdTe device with CdTe film thickness less than 1 um [64]. The energy conversion efficiencies of these devices under different white LED sources along with CCT values of the illuminating sources are listed in Table 4. As can be observed, the efficiency values obtained under different white LED sources vary from 13.55% to 14.98% for the CZTSSe device and 16.73% to 19.02% for the CdTe device. A comparative picture is presented in Figure 4.4 (a) and (b), which shows the

relative efficiency enhancement obtained by taking the lowest efficiency values of CZTSSe and CdTe device in Table 4 as references respectively. The trend is similar for both devices and the observed trend is in fact very much in accordance with the photon yield vs. CCT characteristics of these devices which are plotted in Figure 4.4(c). This indicates that photon yield can describe how a specific PV converter's efficiency can vary depending on CCT value of the white LED source. However for a generalized description, CCT of the white LED source needs to be correlated with the conversion efficiencies of PV converters having different material bandgaps. In Figure 4.4(d), the maximum efficiency limit for different material systems are calculated and plotted as a function of CCT values of these practical white LED sources. As can be observed, for different CCTs of the white LED source, efficiency of single-junction PV devices can vary by about 3.8% to 9.5% depending on absorber material.

4.1.2 Generalized Description Based on Theoretically Modeled Spectra

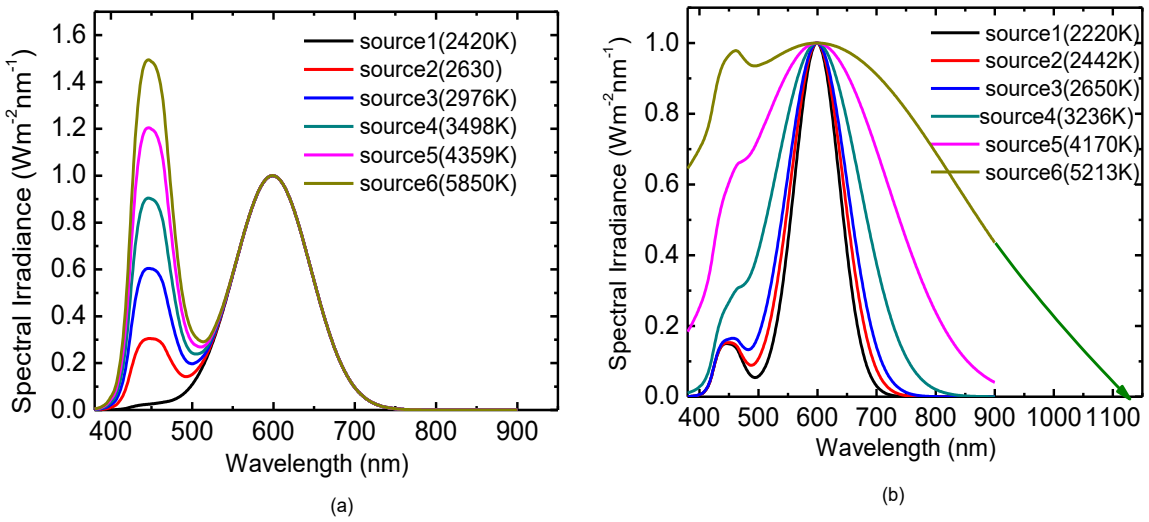

Figure 4.5 : Spectral Irradiance of reference spectra (CCT values shown in parentheses) generated (a) by varying peak intensity of blue emission while keeping main emission linewidth constant and (b) by varying linewidth of main emission while keeping peak intensity of blue emission constant.

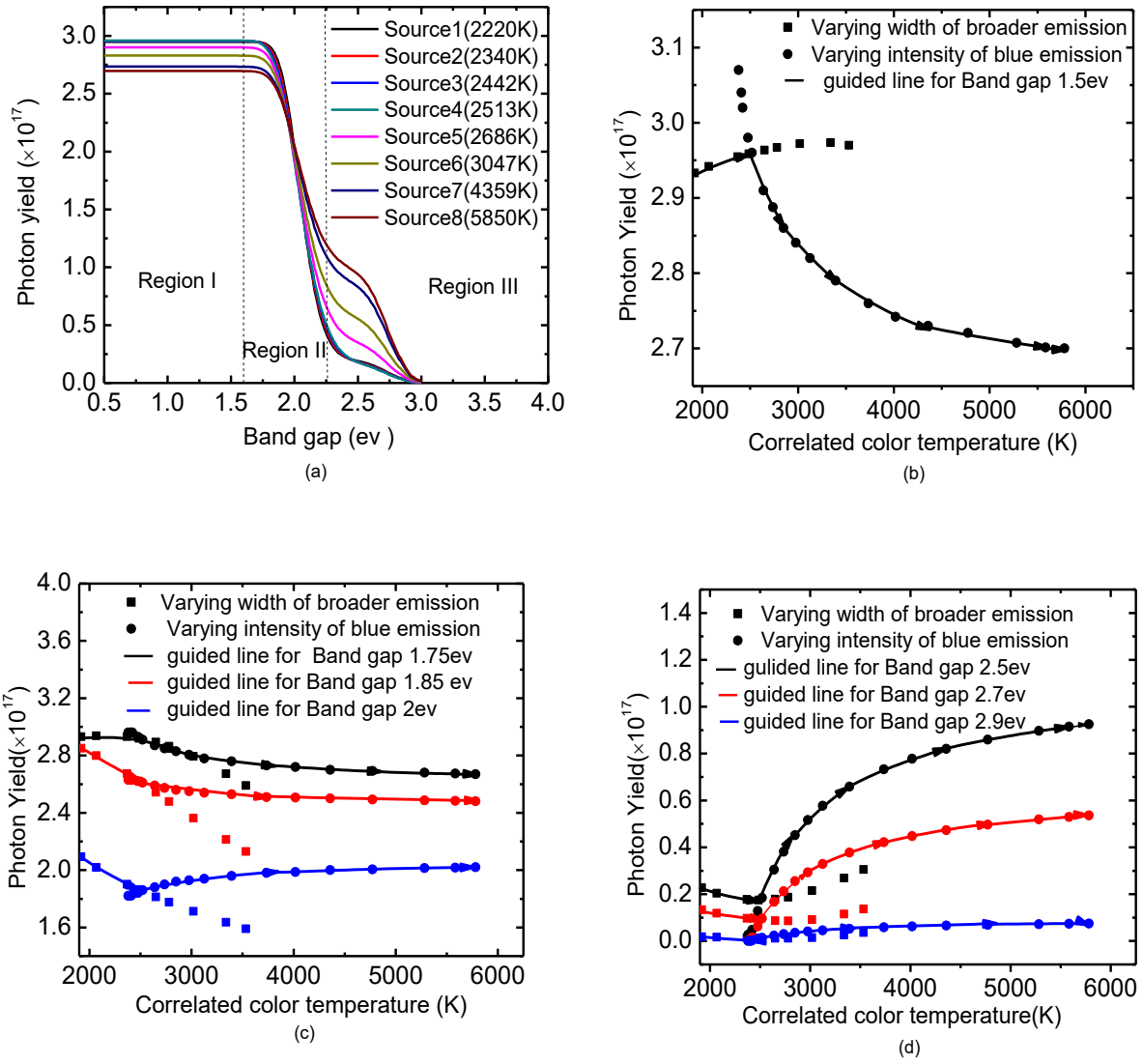

Figure 4.6 : (a) Photon yield as a function of material bandgap for the generated reference set of spectra having intensity of 1000W/m^2; photon yield vs. CCT characteristics for different material bandgaps representing (b) region I (c) region II (d) region III (circle and square for spectra of fig. 4(a) and (b) respectively and solid line for expected commercial white LED spectra).

The observed behavior of PV converter under different white LED sources is generalized by theoretically modeled spectra. The spectra are generated by varying relative intensity of the blue emission peak (I_B) and linewidth ($\Delta\lambda$) of the broader emission centered at 600 nm one at a time which correspond to the CCT values ranging from 2220K to 5850K. For the first set of spectra (Figure 4.5(a)), peak intensity of blue emission is increased from 2% to 150% of the main emission peak by keeping $\Delta\lambda$ unchanged, thereby resulting in CCT variation from 2420K to 5850K. The second set of spectra in Figure 4.5(b) are

generated by varying Δλ from 90nm to 550nm while keeping peak blue emission intensity constant, thereby resulting in CCT values ranging from 2220K to 5213K.

To have an estimate of the fraction of light absorbed by an ideal PV converter under these spectra, photon yields are calculated and plotted in Figure 4.6(a). As can be observed, for all the spectra the photon yield (PY) remains invariant with bandgap as it varies from 0.5eV to 1.5eV. However, PY decreases sharply for material bandgaps residing between 1.5eV and 2.25eV, and then decreases at a less steep slope for bandgaps larger than 2.25eV. Based on these observations, three characteristic regimes labeled as Region I, II and III, have been identified in Figure 4.6(a).

To establish the general relation between PY and CCT in these three regimes, photon yields are next calculated for different bandgaps of the PV absorber material. For Region I, a material bandgap of 1.5eV is considered and the corresponding photon yields are calculated and plotted for LEDs having different CCT values. As shown in Figure 4.6(b), both positive and negative correlations are obtained between PY and CCT, depending on whether Δλ or I_B is increasing. This behavior is better explained with respect to the fraction of blue in the corresponding spectrum, which actually increases both with the increase of I_B and decrease of Δλ. As the blue emission corresponds to a relatively high energy of the incident photon, an increase in the fraction of blue effectively reduces the number of photons per unit energy, thereby reducing the overall photon flux that can be absorbed by the PV device. The solid line shown in Figure 4.6(b) represents the PY vs. CCT characteristics expected for the commercial white LED spectra considered in this study. It is noteworthy that this trend is qualitatively similar to the previously obtained PY vs. CCT characteristics (Figure 4.4(c)) of CZTSSe and CdTe devices, for which the absorber layer bandgaps were 1.1eV and 1.45eV respectively, both residing in Region I. Because PY is independent of bandgap in Region I, similar characteristics are expected for PV converters having any other material bandgap within this region. This is evident from Figure 4.4(d) also, which shows similar qualitative dependence of efficiency limits on CCT for CZTSSe, AlGaAs, crystalline Silicon(c-Si) and GaAs materials, all of which have bandgaps within Region I.

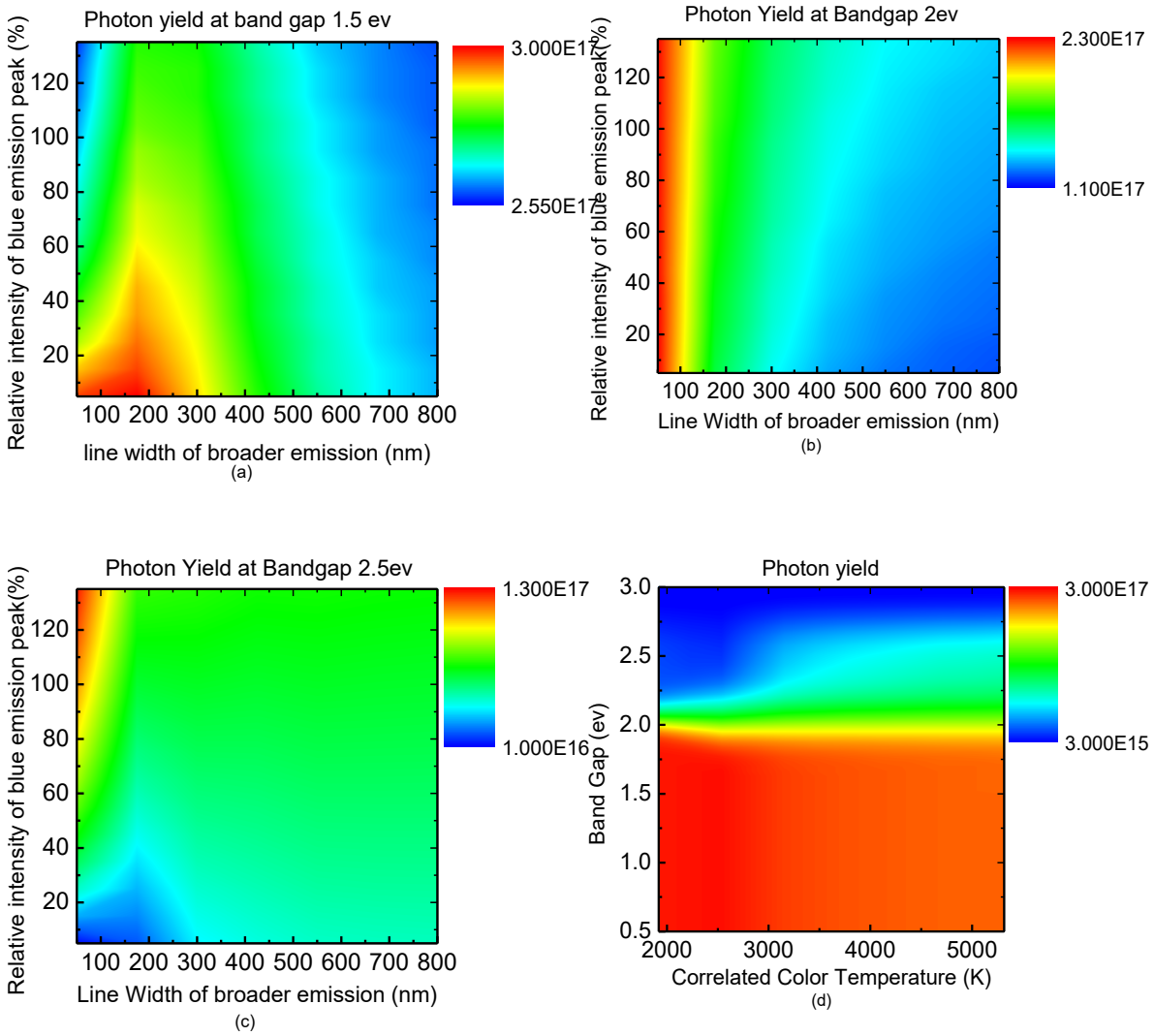

Figure 4.7 : Photon yield as a function of main emission peak's linewidth and blue emission peak's intensity of reference spectra(intensity 1000W/m^2) for absorbing material of (a) band gap 1.5ev (b) band gap 2ev and (c) band gap 2.5ev and (d)Photon yield as a function of spectra's CCT and band gap of the absorbing material

The dependence of photon yield on the illuminating spectrum is further illustrated in Figure 4.6(c) and (d) for material bandgaps corresponding to Region II and III respectively. The solid lines shown in these figures indicate the characteristics expected from operation under commercial white LED sources. For materials of high bandgap, the photon conversion efficiency, and hence the photon yield is expected to increase if there is an increase in the number of higher energy photons in the incident spectrum. Therefore enhancement of the percentage of blue in the white LED source, resulting from either increase of I_B or decrease of $\Delta\lambda$, should increase the photon yield for materials of high

bandgap. Such a trend is particularly evident in Region III, where material bandgaps ranging from 2.5eV to 3eV can absorb only the high energy photons residing in the vicinity of the blue region of the emission spectrum. Consequently for material bandgaps of 2.5eV or higher, PY tends to increase as the illuminating source tend to be more cool white in nature. Based on the choice of material bandgap in Region II, the dependence of PY on CCT exhibits characteristics similar to those of Region I or III. As has been shown by the solid line in Figure 4.6(c), for a relatively smaller bandgap of 1.75eV, PY tends to remain nearly invariant with CCT for up to 2500 K and then decrease monotonically as CCT further increases, a characteristic similar to that of Region I. On the contrary, for higher values of bandgap, such as for Eg = 2eV as has been considered in the plot, the trend appears to be in accordance with the characteristics observed in Region III. It is noteworthy that in the efficiency limit vs. CCT plot of Figure 4.4(d), similar characteristic trend is obtained with GaInP, for which a material bandgap of 1.9eV is considered.

A summary of the results obtained for the three regions is illustrated using false color plots in Figure 4.7. The color plots shown in Figures 4.7(a)-(c) present the dependence of PY on I_B and $\Delta\lambda$, for specific bandgaps of the PV absorber material representing region I, II and III respectively. As can be observed, low linewidth of the main emission peak of the white LED source is preferred for all bandgaps of the PV absorber material in order to attain high photon yields. On the other hand, high intensity of the blue emission peak is desirable for the PV materials having bandgaps of 2eV or higher. The relation of PY with material bandgap and CCT is shown in Figure 4.7(d), which clearly illustrates the three regions signifying the dependence of photon conversion efficiency on CCT of the illuminating spectra. The results shown here indicate that for absorber materials having bandgaps smaller than 2eV, higher photon conversion efficiency is expected for operation under warm glow white LEDs. On the contrary, white LEDs emitting cool light are more suitable for PV converters designed with higher bandgap absorber materials.

These results provide necessary guideline for choosing appropriate absorber material for designing the photonic structure operating under white LED sources. Accordingly we have designed the photonic structure with the CdTe device because its active layer CdTe's bandgap is closer to optimal bandgap under white LED sources than that of

CZTSSe material. Moreover since its bandgap resides in region I, the photonic structure is expected to perform better under warm glow white LEDs than cool light white LEDs.

4.2 Design Optimization of Photonic Structure

The first part of this section shows optical power absorption results for all three types of photonic structures considered in this study. In the subsequent part, energy conversion efficiencies of the structured PV devices have been shown for operation under natural and different white LED sources. Based on optimal energy conversion efficiencies under the sources, spectra selective photonic structures have been designed.

4.2.1 Optical Power Absorption by the Photonic Structure

To increase the light absorption and hence conversion efficiency of ultrathin film PV converters we have designed three types of photonic structures (Figure 3.3). The photonic structures have periodic circular holes filled with dielectric i.e. SiO_2 into-

i. both active and window layer (configuration A1)
ii. only active layer (configuration A2) and
iii. only window layer (configuration A3)

We have calculated the fraction of incident power absorbed by the photonic structures by varying dielectric filled circular hole's diameter from 150nm to 350 nm and fractional area (FA) from 20% to 90% of the absorber layer. Figure 4.8 shows absorption spectra of all three configurations at varying diameters keeping fractional area fixed at 30% (Figure 4.8 (a)-(c)) and at 50% (Figure 4.8 (d)-(f)). As can be observed, light absorption increases for all the photonic structures compared to the bare CdTe device in the wavelength range of 400-700 nm which is the useful spectrum region of all illuminating sources. Also it can be seen that , absorption changes very small with the variation of

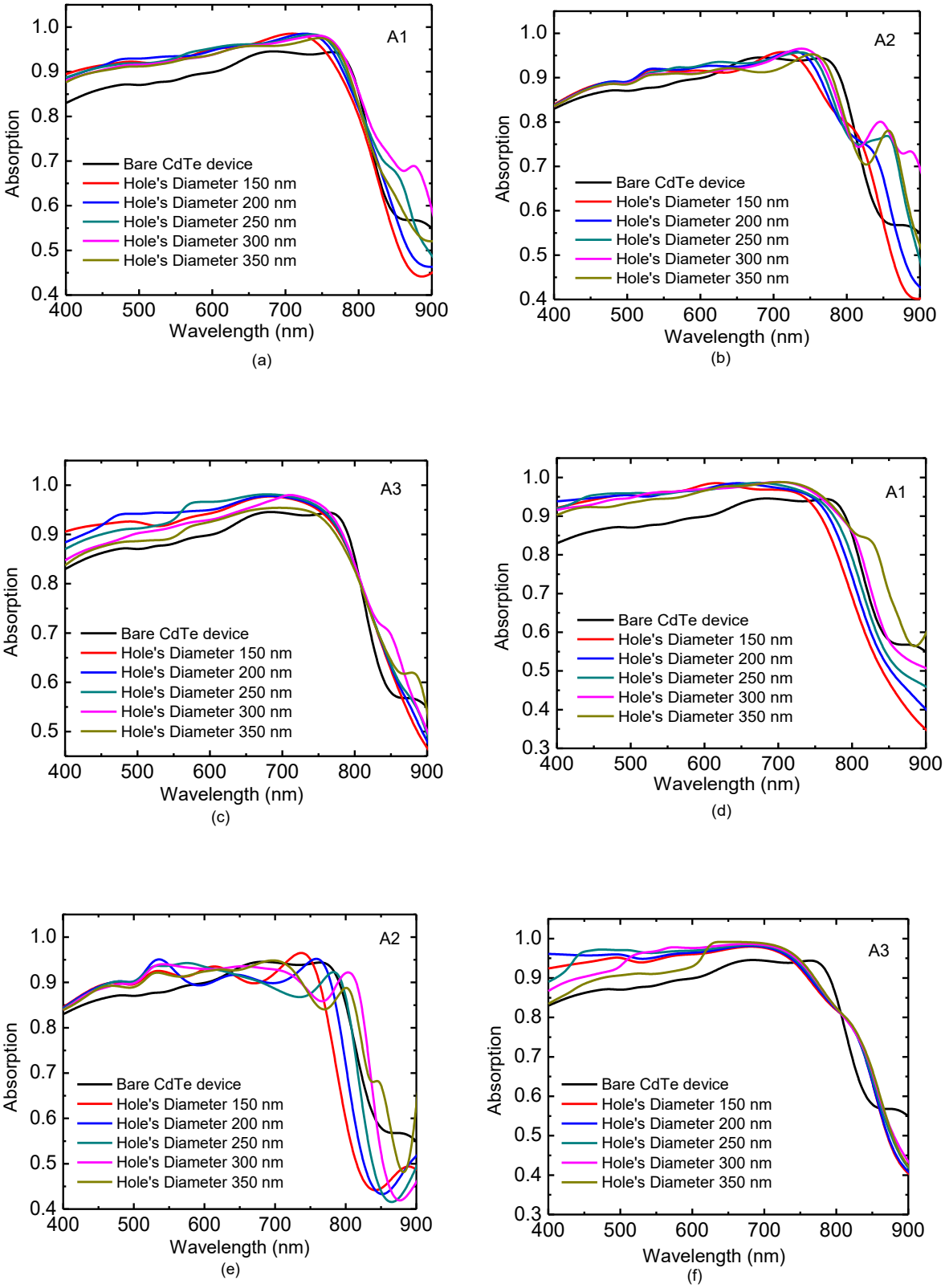

Figure 4.8 : Absorption spectra with varying SiO_2 filled hole's diameter at fractional area of 30% for (a) configuration A1 (b) configuration A2 (c) configuration A3 and fractional area of 50% for (d) configuration A1 (e) configuration A2 and (f) configuration A3

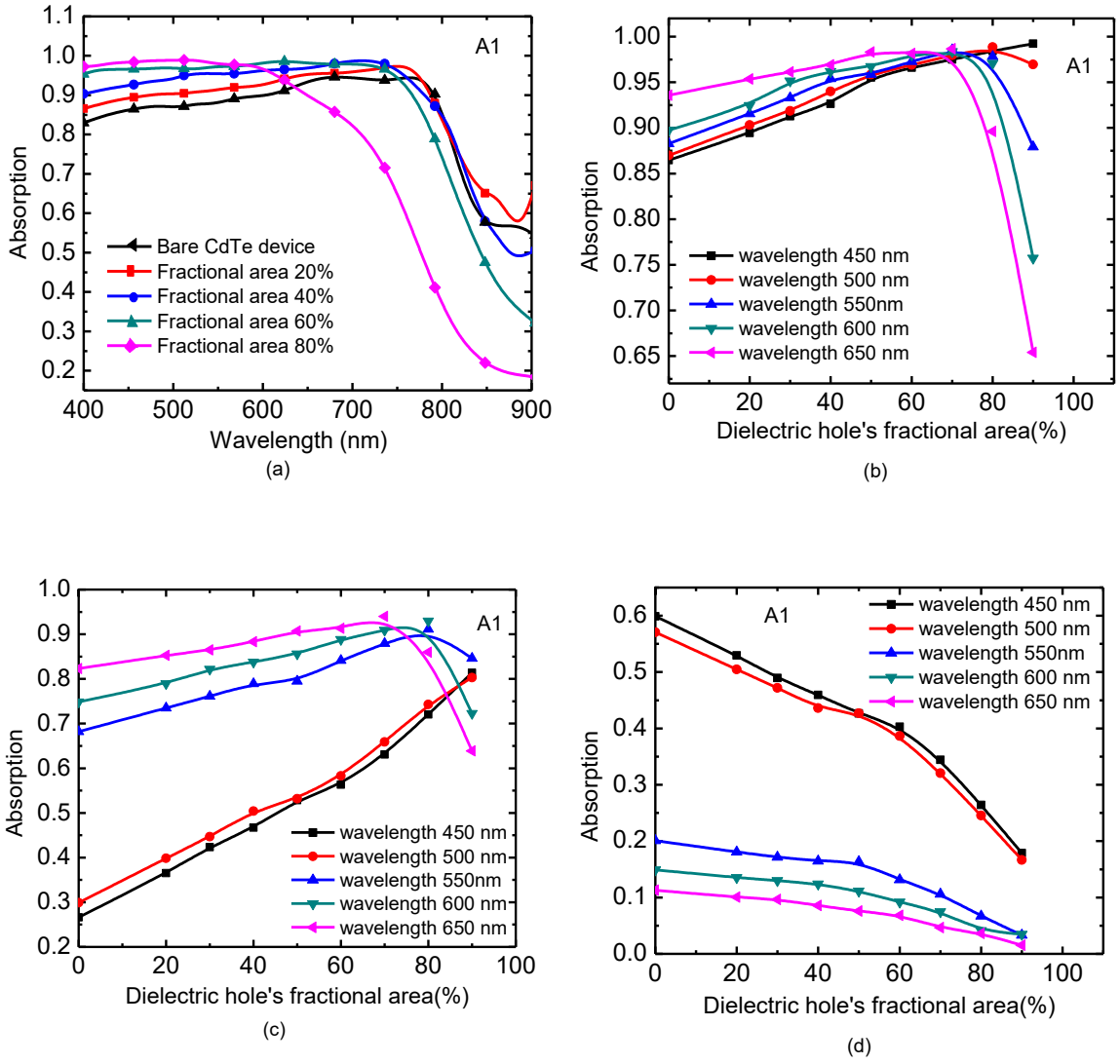

Figure 4.9 : (a) Absorption spectra at varying fractional area of SiO_2 holes and absorption as a function of fractional area at different wavelengths for (b) whole structure (c) active (CdTe) layer (d) window (CdS) layer for the photonic structure A1

dielectric hole's diameter. So we have considered a fixed experimentally realizable diameter of 250 nm of the dielectric filled holes for further study[16], [30].

For configuration A1, Figure 4.9(a) shows absorption spectra for varying fractional area at fixed diameter of 250 nm and Figure 4.9 (b) shows absorption vs. FA plot at some particular wavelengths in the useful wavelength range. As can be seen in figure 4.9(b), absorption is relatively low at very high and low FA of dielectric filled holes (bare PV device denotes zero fractional area) because photonic structures with very low and high

FA act almost as solid material layer and cannot effectively trap light by multiple light scattering and wave interference as patterned structures. Besides absorption by the whole photonic structure, light absorption in active layer (CdTe) and window layer (CdS) have been calculated individually for configuration A1 and plotted in Figure 4.9(c) and (d). By the photonic structures we want to maximize light absorption in the active layer and minimize absorption in window layer. As shown in Figure 4.9 (c) and (d), in bare PV device, high energetic photons of wavelength less than 500 nm is mostly absorbed in window layer and relatively low energetic photons of wavelength greater than 500 nm is absorbed in active layer. After introducing SiO_2 filled holes, overall absorption of high energetic photons has been increased and most importantly this increase results from increased absorption in active region whereas absorption in the window layer has been decreased. The phenomenon can be better explained by the electric filed distribution of the downward propagating light wave in xz plane shown in Figure 4.10 (a) and (b). As shown in Figure 4.10 (a), for bare device at an excitation of 500 nm, electric field intensity decreases rapidly while propagating from window layer to active layer, hence almost all photons are absorbed in the window layer. Dielectric holes in the window layer distribute electric filed in the active layer as shown in Figure 4.10(b), therefore absorption in the active layer increases. So it can be said that dielectric holes in the window layer cannot localize light greatly in this layer, rather it passages and localizes light to the active layer due to very low thickness of the window layer (thickness 100 nm). However, higher wavelength lights are effectively confined by dielectric holes in the relatively

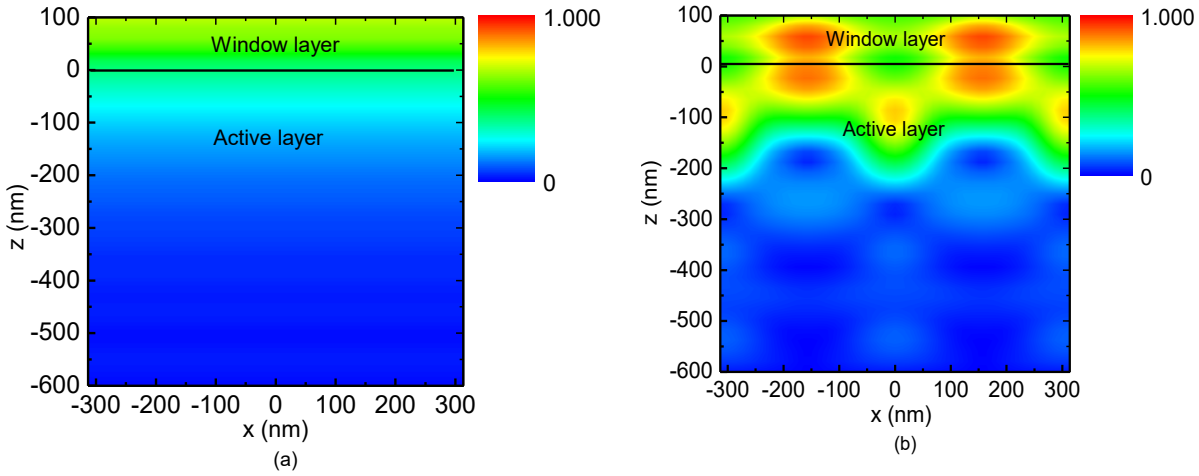

Figure 4.10 : Electric filed distribution in the xz-plane at an excitation of 500 nm for (a) bare CdTe device and (b) configuration A1 with fractional area 50%

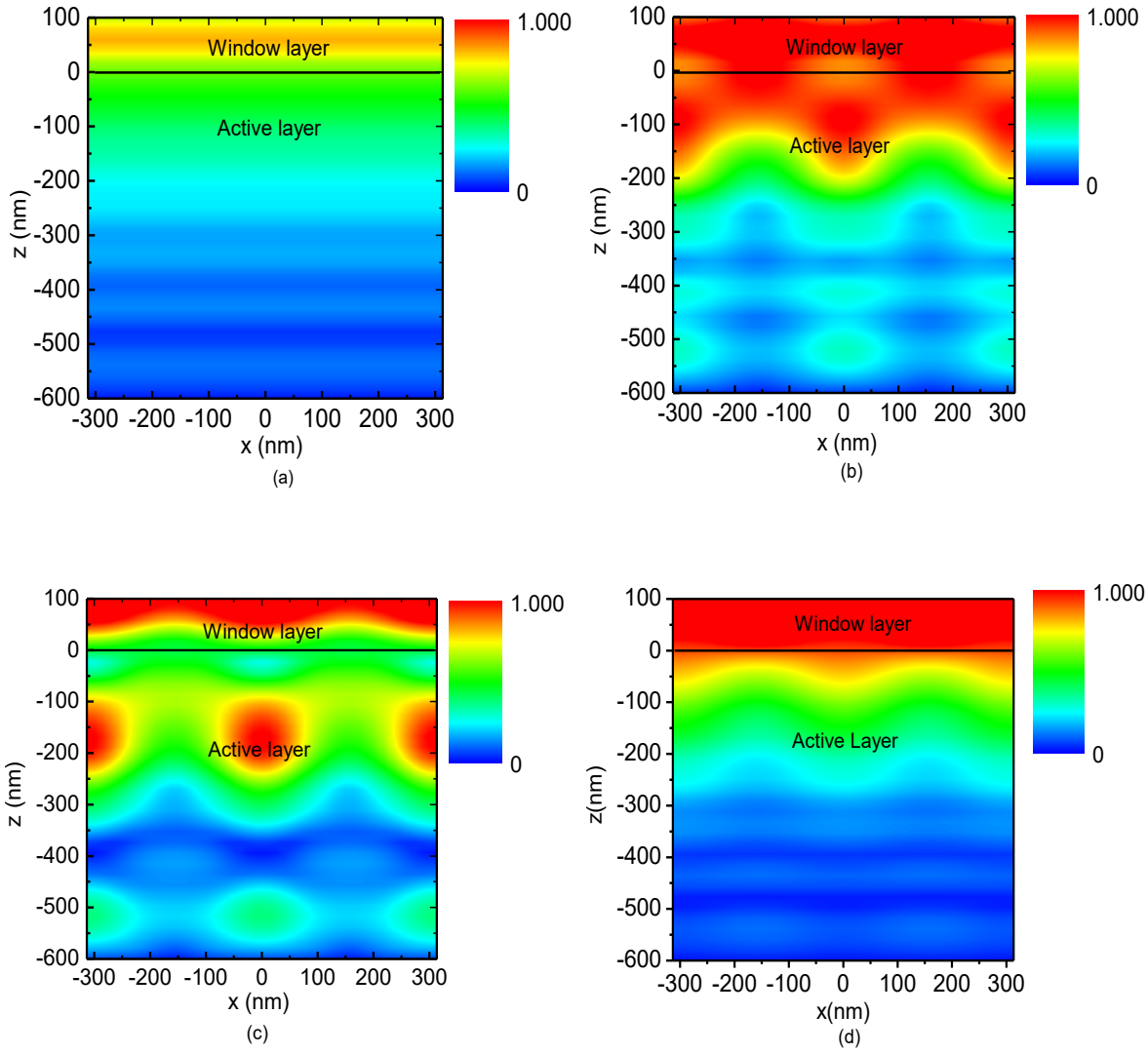

Figure 4.11: Electric filed distribution in the xz-plane at an excitation of 600 nm for (a) bare CdTe device (b) configuration A1 (c) configuration A2 and (d) configuration A3 with fractional area 50%

thicker active layer (thickness 600 nm), as shown by the electric field distribution at an excitation of 600 nm in figure 4.11(b). As a result absorption of lower energetic photons increases in active layer when dielectric holes are introduced. At very high fractional area this absorption falls as can be seen in Figure 4.9(c) when amount of absorber material is greatly reduced.

The effect of dielectric hole's fractional area on light absorption has also been studied for configuration A2 and plotted in Figure 4.12 (a) to (d).As can be seen from Figure 4.12(b),

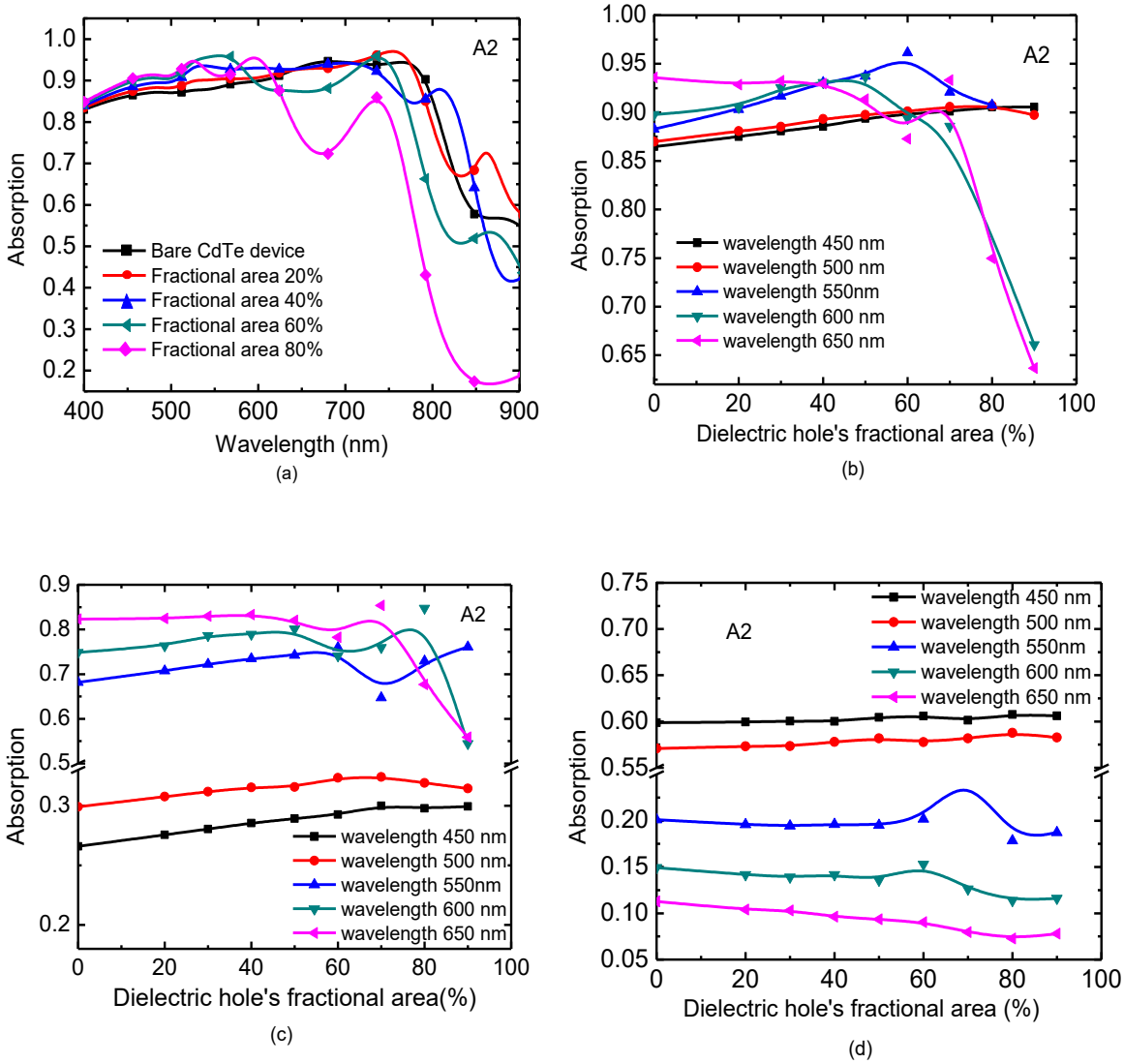

Figure 4.12 : (a) Absorption spectra at varying fractional area of SiO_2 holes and absorption as a function of fractional area at different wavelengths for (b) whole structure (c) active (CdTe) layer (d) window (CdS) layer for the photonic structure A2

absorption of high energetic photons in the photonic structure does not change significantly with varying FA because these structures don't contain dielectric holes in the window layer. Absorption of lower energetic photons in the active layer also remains almost invariant with fractional area as shown in Figure 4.12(c) because higher wavelength lights are not highly localized in the active layer when the upper window layer is solid. It is evident from electric field distribution of 600 nm light wave for configuration A2, shown in Figure 4.11(c). This high wavelength light cannot be effectively localized in the active layer for configuration A2 like configuration A1.

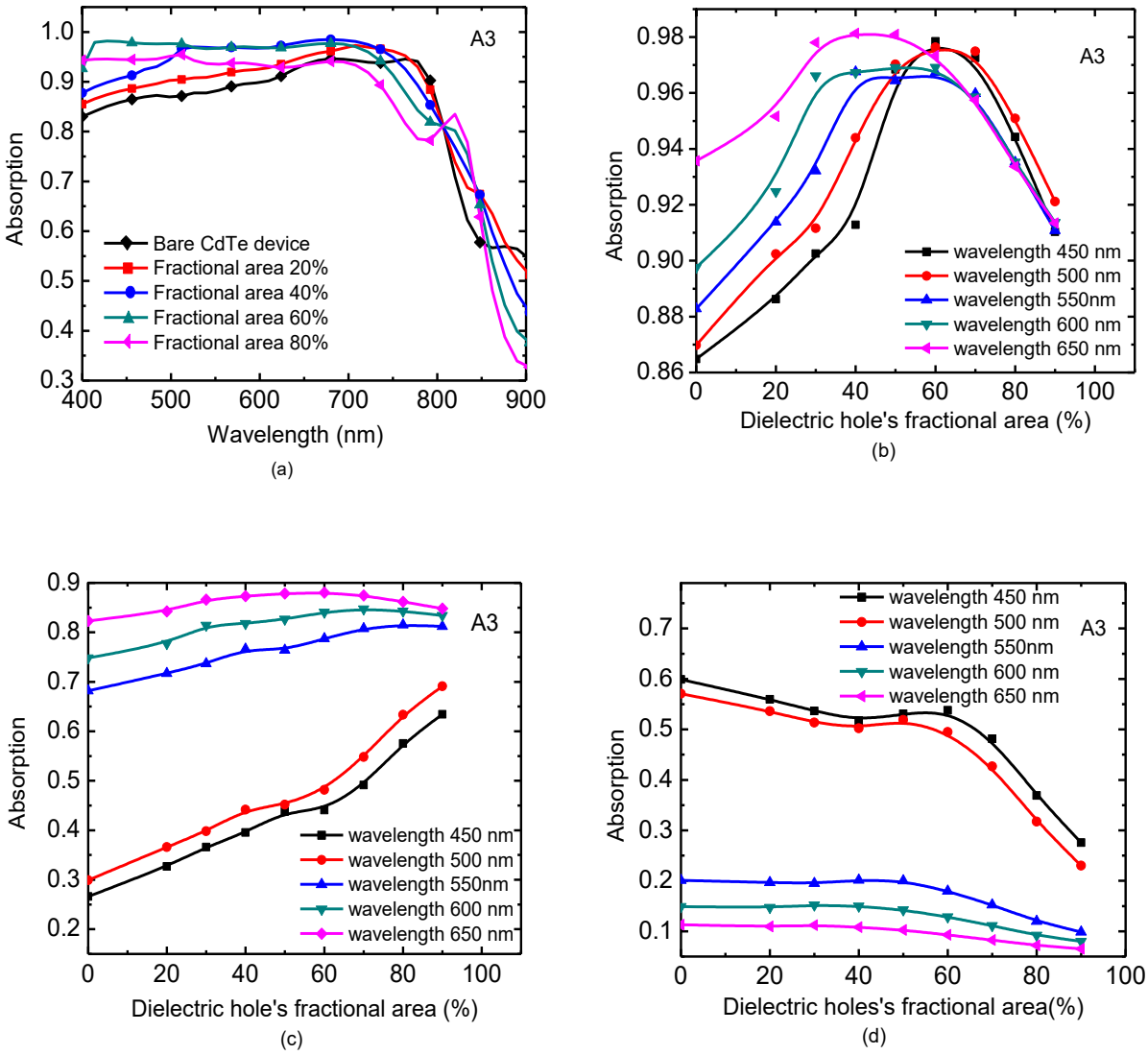

Figure 4.13: (a) Absorption spectra at varying fractional area of SiO_2 holes and absorption as a function of fractional area at different wavelengths for (b) whole structure (c) active (CdTe) layer (d) window (CdS) layer for the photonic structure A3

Similar studies have been done for configuration A3 and results are shown in Figure 4.13 (a) to (d). As can be seen from Figure 4.13(b), similar to configuration A1 in this photonic structure absorption of high energetic photons is increased due to increased absorption in the active layer as shown in 4.13 (c). Despite bare active layer, absorption of lower energetic photons increases little in the active layer as observed from figure 4.13(c) because structured upper window layer causes light confinement in the active layer which is also observed from the electric field distribution at an excitation of 600 nm for configuration A3 in Figure 4.11 (d).

We have also integrated absorption in the active layer over the useful wavelength range of 400-720 nm for all three configurations and compared the values with that of bare CdTe device. A thin film PV device with amorphous silicon active layer patterned as 2D photonic crystal membrane was previously reported to have 28% increased integrated absorption compared to the unpatterned stack [87]. In our study, for configuration A1, maximum 40% increase in integrated absorption compared to bare CdTe device is obtained for 80% FA of dielectric holes. For configuration A2, maximum integrated absorption is only 4.5% relative to bare device at 40% FA. For configuration A3, the integrated absorption increases with increasing FA of dielectric holes and the maximum obtained value is 30%.

4.2.2 Validation of Electrical modeling

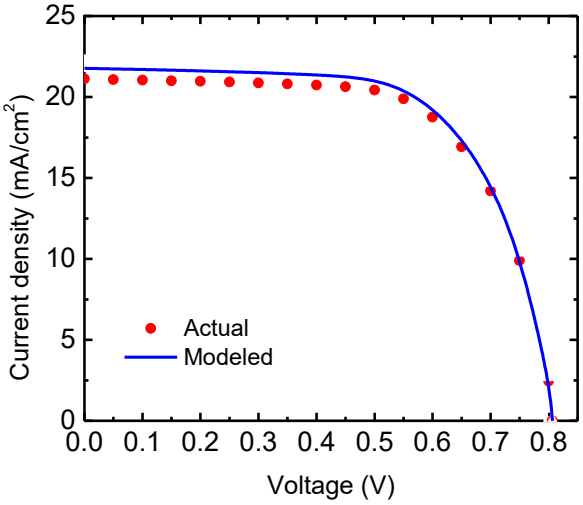

Figure 4.14: Current density and voltage relation for the modeled structure along with actual photonic structure of configuration A1's values under solar AM 1.5 spectrum

In electrical simulation, we have modeled the dielectric holes by the resistance of the containing absorber layer. Since the holes will decrease drift-diffusion current density, we have increased the layer's resistance according to (3.13). The model is validated against output characteristics of the actual photonic structure, the current density vs. voltage (J-V) characteristics of which is shown along with the modeled one in Figure 4.14. Under solar spectrum, short circuit current density of our considered CdTe device was 22.4mA/cm^2. As can be seen in Figure 4.14, after introducing holes it decreases to 21.1mA/cm^2 for the

actual photonic structure which means 5.8% decrease in bare device's current density. On the other hand, for our modeled structure current density has decreased by 3.12% with a short circuit current density of 21.7mA/cm^2. The probable reason of these small discrepancies is non-uniform distribution of electric field at the edge of dielectric holes due to fringing effect which we have ignored in our modeling.

4.2.3 Energy Conversion Efficiency of the Photonic Structure

In order to design spectra selective photonic structures which will be able to maximize conversion efficiency of the PV device under the illuminating source, energy conversion efficiencies of three types of photonic structures have been calculated under standard AM 1.5 solar spectrum and commercially available white LED sources using the electrical modeling.

For configuration A1, energy conversion efficiencies have been calculated varying fractional area of dielectric holes from 0% (bare CdTe device) to 90% considering illumination under solar spectrum and Philips (2492K) LED source and the obtained I-V parameters are listed in Table 5. As can be observed, energy conversion efficiency of the photonic structure decreases from 11.7% to 5.3% for AM 1.5 solar spectrum and it decreases from 19% to 9% for the LED source while increasing FA which is shown in Figure 4.15 (a) as well. Again current density vs. FA characteristics plotted in Figure 4.15(b) shows that current density of the photonic structures decreases with increasing FA due to interference of charge carriers with dielectric holes in active and window layer. Besides, as fractional area of dielectric holes increases, the containing layers become more resistive and fill factor of the device drops as can be observed from Figure 4.15(b) as well. Due to these dual effects, overall conversion efficiency of the photonic structure decreases. Similar studies have been made for configuration A2 and the results are summarized in Table 6 and shown in Figure 4.16(a) and (b). Figure 4.16 (a) shows similar FA dependence of power conversion efficiency for photonic structures of configuration A2 like A1 due to decreased current density and fill factor with increasing FA of dielectric holes in the active layer as observed from Figure 4.16(b).

Table 5: I-V parameters of configuration A1 at different fractional areas of dielectric holes under solar and Philips (2492K) sources

Fractional Area(%)	AM 1.5 solar spectrum				Philips (2492K) white LED			
	J_{sc}(mA/cm^2)	V_{oc}(V)	FF(%)	η(%)	J_{sc}(mA/cm^2)	V_{oc}(V)	FF(%)	η(%)
0(Bare)	22.33	0.79	66.8	11.7	33.75	0.82	68.2	19.0
20	22.31	0.81	65.7	11.6	33.26	0.83	65.7	18.6
30	21.17	0.81	65.6	11.3	32.48	0.83	65.6	18.4
40	21.24	0.82	65.1	11.3	33.0	0.84	65.1	18.3
50	20.1	0.82	65.0	10.7	31.45	0.85	65.0	17.4
60	20.0	0.83	64.0	10.6	30.7	0.85	64.0	16.8
70	18.5	0.83	62.8	9.7	29.6	0.86	62.8	15.8
80	16.5	0.83	59.8	8.3	28.9	0.86	59.8	14.5
90	10.6	0.84	58.7	5.3	18.29	0.86	58.7	8.9

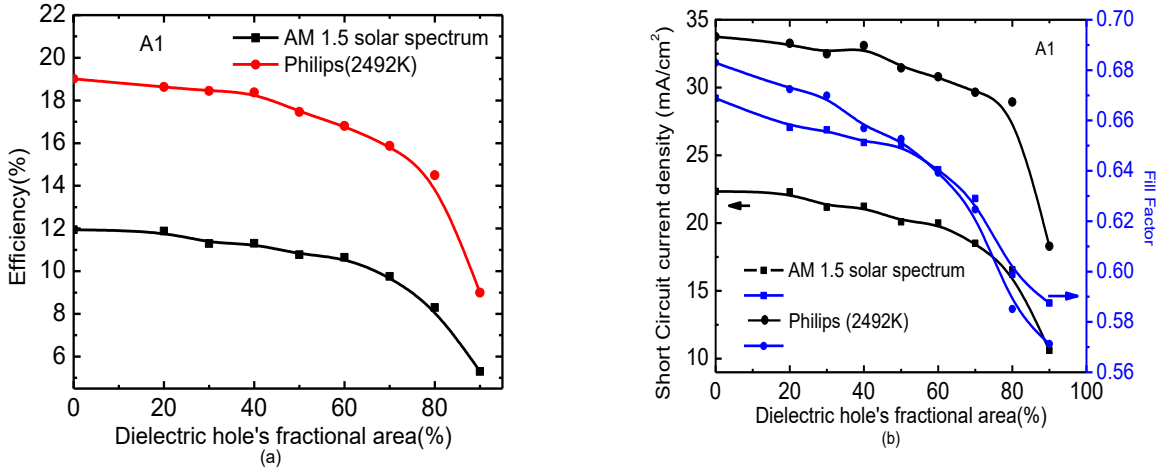

Figure 4.15 : (a) Efficiency as a function of fractional area and (b) short circuit current density and Fill factor as a function of fractional area for the photonic structure A1 under AM 1.5 solar spectrum and Philips(2492K) LED source.

For the photonic structure of configuration A3, varying fractional area of dielectric holes energy conversion efficiency can be increased up to 13.22% from bare device's efficiency of 11.7% under AM 1.5 solar spectrum and up to 20.84% from bare device's efficiency of 19% under Philips (2492K) Led source. A summary of the I-V parameters under these

Table 6: I-V parameters of configuration A2 at different fractional areas of dielectric holes under solar and Philips (2492K) sources

Fractional Area(%)	AM 1.5 solar spectrum				Philips (2492K) white LED			
	J_{sc}(mA/cm^2)	V_{oc}(V)	FF(%)	η(%)	J_{sc}(mA/cm^2)	V_{oc}(V)	FF(%)	η(%)
0(Bare)	22.33	0.79	66.8	11.7	33.75	0.82	68.2	19.0
20	21.74	0.80	65.4	11.5	31.74	0.83	66.8	17.6
30	20.35	0.80	65.0	10.7	30.7	0.83	65.9	16.8
40	19.91	0.81	64.6	10.4	30.88	0.83	65.1	16.8
50	18.0	0.81	64.7	9.5	28.55	0.83	64.5	15.4
60	17.9	0.82	63.9	9.4	27.8	0.84	63.5	15.0
70	16.95	0.83	62.8	8.8	27.4	0.85	62.5	14.6
80	16.32	0.84	59.8	8.2	28.5	0.86	58.9	14.9
90	11.69	0.85	59.8	6.0	21.36	0.87	57.9	10.8

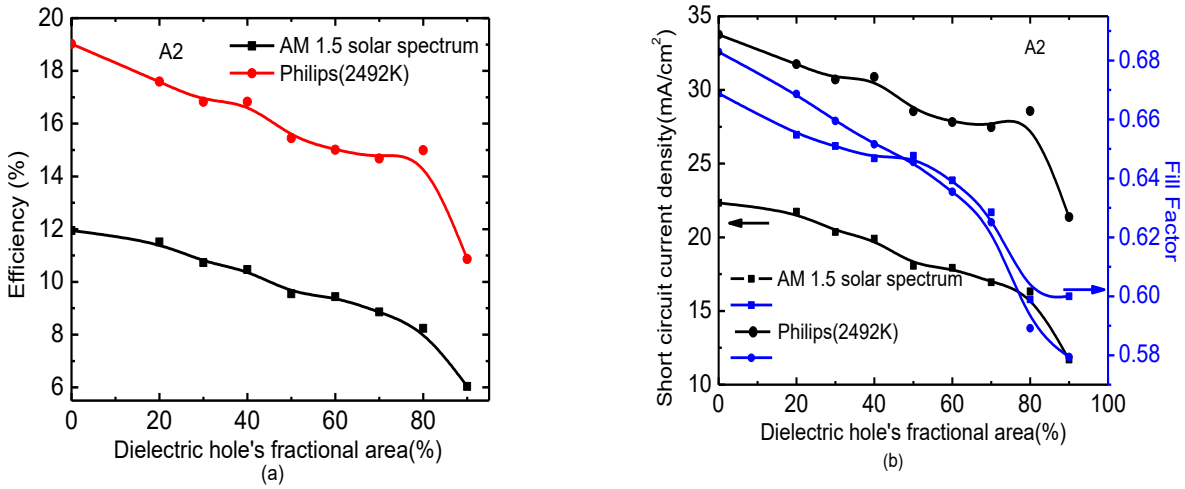

Figure 4.16 : (a) Efficiency as a function of fractional area and (b) short circuit current density and Fill factor as a function of fractional area for the photonic structure A2 under AM 1.5 solar spectrum and Philips(2492K) LED source.

two sources are listed in Table 7 and a comparative picture of the obtained conversion efficiencies is presented in Figure 4.17 (a). It is noteworthy that, this trend is qualitatively similar to the short circuit current density vs. FA characteristics shown in Figure 4.17(b) and previously obtained absorption vs. FA characteristics of this configuration (Figure 4.13(b)). The results shown here indicate that, for this photonic structure short circuit

Table 7: I-V parameters of configuration A3 at different fractional areas of dielectric holes under solar and Philips (2492K) sources

Fractional Area(%)	AM 1.5 solar spectrum				Philips (2492K) white LED			
	J_{sc}(mA/cm^2)	V_{oc}(V)	FF(%)	η(%)	J_{sc}(mA/cm^2)	V_{oc}(V)	FF(%)	η(%)
0(Bare)	22.33	0.79	66.8	11.7	33.75	0.82	68.2	19.0
20	23.42	0.80	66.5	12.6	34.88	0.82	68.4	19.7
30	23.88	0.80	66.5	12.8	35.74	0.83	68.6	20.3
40	24.44	0.80	66.6	13.1	36.71	0.83	68.3	20.8
50	24.5	0.80	66.6	13.2	36.52	0.83	68.5	20.7
60	24.3	0.80	66.7	13.1	36.07	0.83	68.5	20.5
70	24.4	0.80	66.7	13.1	36.25	0.83	68.5	20.6
80	23.9	0.80	66.7	12.9	34.84	0.82	68.7	19.8
90	23.0	0.80	66.7	12.4	33.22	0.82	68.7	18.9

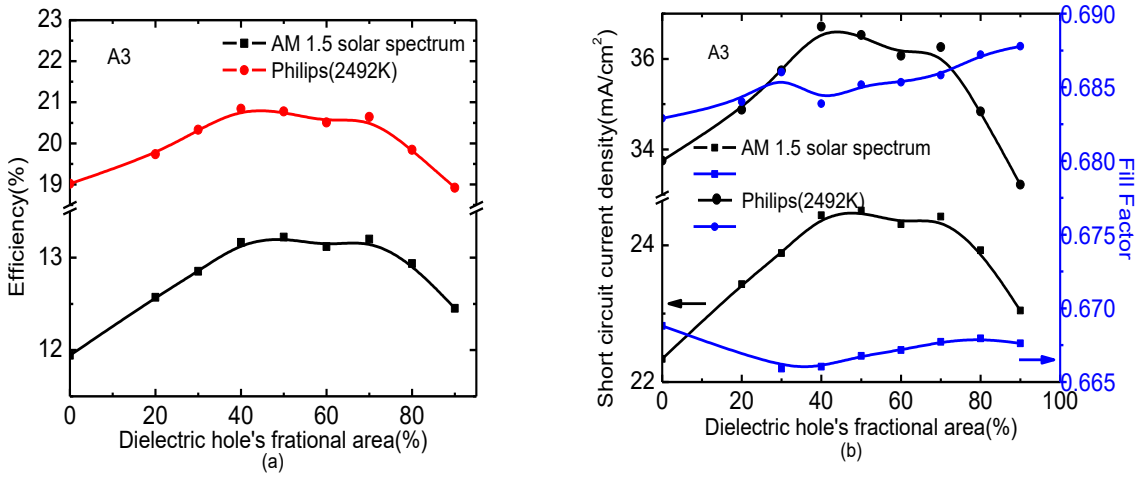

Figure 4.17 : (a) Efficiency as a function of fractional area and (b) short circuit current density and Fill factor as a function of fractional area for the photonic structure A3 under AM 1.5 solar spectrum and Philips(2492K) LED source.

current density increases with increased light absorption i.e. photogenerated electron-hole pairs. Dielectric holes in window layer cannot affect significantly on transportation and collection of charged carriers towards the respective electrode since drift velocity of the carriers is quite high in the highly doped thin window layer. Moreover, since active layer does not contain any dielectric holes, device resistance does not change much with FA

which is also observed from FF vs. FA plot from Figure 4.17(b). As a result energy conversion efficiency closely follows photo current. These obtained results are comparable to the performance of a structured thin film AlGaAs/GaAs solar cell, theoretical conversion efficiency of the PV structure was enhanced upto 9.383% from planar cell's efficiency of 7.432% under solar spectrum using 2D photonic structures at the front surface of the cell [88].

In summary, although optical power absorption in the active layer have been enhanced for all three types of photonic structures, for configuration A1 and A2, motion of photo-generated carriers towards the respective electrodes are inhibited by the dielectric filled holes in the active layer, so overall current density and energy conversion efficiency decreases from the bare PV device for these two structures. Only for configuration A3 that contains dielectric filled holes only in window layer, energy conversion efficiency has been increased from the bare CdTe device. So in order to design spectra selective photonic structure, configuration A3 has been selected and its performance has been evaluated under different commercially available white LED sources.

4.2.4 Spectra Selective Photonic Structure Design

For configuration A3, energy conversion efficiencies have been calculated under different white LED sources. The conversion efficiencies obtained are listed in Table7 and energy conversion efficiency vs. FA characteristics under the sources is plotted in Figure 4.18. As expected the photonic structure performs better under warm glow white LEDs since the absorber material of the structure is CdTe having bandgap less than 1.5eV. The figure also depicts that energy conversion efficiency of the photonic structure enhances from the bare PV device for all illuminating sources. However the fractional area of dielectric holes at which peak efficiency is recorded is different depending on the LED source. For warm glow white LEDs like Philips (2492K) and Philips (2894K) having minimum fraction of blue, efficiency reaches maximum at 40% FA since absorption of relatively high wavelength lights i.e. low energetic photons is maximum close to this FA (Figure 4.13(b)). On the contrary, since Ledtech (5833K) emitting cool light have maximum fraction of blue, efficiency under the LED source maximizes at 70% FA where low wave-

Table 8: Conversion efficiencies of configuration A3 at different fractional areas under commercial white LED sources

Fractional area (%)	Efficiency, η (%) under Philips(2492K)	Efficiency, η (%) under Philips(2894K)	Efficiency, η (%) under Ledtech (5833K)
0(Bare)	19.01	18.44	16.72
20	19.73	19.57	17.96
30	20.33	20.24	18.8
40	20.84	20.82	19.53
50	20.77	20.84	19.96
60	20.5	20.6	19.81
70	20.62	20.84	20.35
80	19.84	20.14	20.17
90	18.91	19.28	19.64

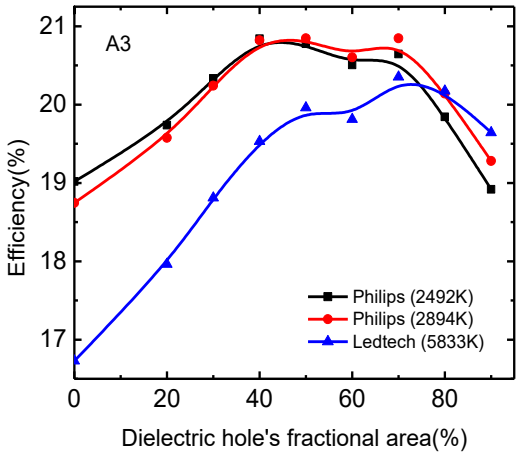

Figure 4.18: Efficiency as a function of fractional area under different white LEDs for the photonic structure A3.

length lights or high energetic photons are more effectively absorbed (Figure4.13(b)). However as shown in Figure 4.17(a), a relatively flat efficiency vs. FA characteristics is obtained under AM1.5 solar illumination and efficiency is high over theFA range of 50% to 70% due to broad band emission spectrum of solar irradiation. The results provide a guideline to design spectra selective photonic structures for optimized operation under different sources.

CHAPTER 5
Summary and Future Work

5.1 Summary

This thesis provides an in-depth study of photonic structures for spectrum-dependent energy harvesting of photovoltaic devices. These studies require increased attention as mm-scale electronics become ubiquitous in our society. Traditional photonic structures are not optimized for photovoltaic energy harvesting from ambient light because they are designed for solar radiation whose spectrum is very much different from artificial sources. The material and design of the photonic structures must be optimized for artificial sources for efficient energy harvesting from ambient light.

In the initial part of this work, appropriate absorber material of the photonic structure has been chosen by evaluating efficiency limit of single-junction photovoltaic devices for different absorber materials and identifying optimal absorber bandgaps under natural and artificial light sources. Moreover due to wide spread use of white LED sources, the dependence of photovoltaic energy conversion efficiency on spectral characteristics of these sources has been studied in detail. Considering illumination by different commercially available white LED sources, energy conversion efficiency of an experimentally reported CZTSSe and CdTe device is estimated based on numerical simulation of Poisson's and continuity equations under optical generation-recombination conditions. For a specific PV observer material, the obtained characteristics are found to be intricately related to the correlation between color temperature and photon yield of the illuminating spectrum. The findings have been further generalized for any combination of PV absorber material and white LED spectrum of interest. The established general framework between conversion efficiency of the photovoltaic device and correlated color temperature of the illuminating spectrum indicate that depending on bandgap of the PV absorber material and fraction of blue of the white LED spectrum, both positive and

negative correlations are possible between energy conversion efficiency of the PV device and CCT of the white LED source. Whereas warm glow white LEDs are found to be more conducive for material bandgaps of 2eV or smaller, cool white emitting LEDs should be favored for higher bandgap materials to attain higher conversion efficiencies. The results presented here therefore provide a guideline to correlate absorber material's bandgap with illuminating white LED sources' photometric attributes for obtaining optimal conversion efficiency of the photonic structures under the sources.

In the later part of the work, photonic structure has been designed with the CdTe active layer since its bandgap is closer to optimal bandgap than that of CZTSSe under LED sources. Considering illumination by solar spectrum and commercially available white LED sources, energy conversion efficiency of an experimentally reported CdTe device has been estimated incorporating dielectric filled holes in different layers of the device. For all illuminating sources, performance of the photonic structure having dielectric holes in the window layer is found to be better than all other structures. However, the fractional area of dielectric holes in the window layer for which peak efficiency is obtained is found to be different depending on illuminating sources and for white LED sources, it is related to the photometric attributes i.e. fraction of blue and correlated color temperature of the illuminating LED source. While photonic structure with low fractional area (~40%) exhibits superior performance under warm glow white LEDs, high fractional area of holes (~70%) is more conducive for operation under LED sources emitting cool light. Of course a better performance is found for warm glow white LEDs since the absorber material is CdTe having bandgap less than 2eV. The optimized photonic structure obtained for white LED illumination has been compared with that for solar irradiation and the photonic structure performs well for a wide range of fractional area in between 50% to 70% under AM 1.5 solar irradiation because of its broad emission spectrum.

5.2 Scope of Future Works

This thesis elaborates a relation of energy conversion efficiency of photovoltaic devices with absorber material's bandgap and photometric attributes of white LEDs which can be a useful guideline for designing homojunction, heterojunction or tandem PV devices

suitable for operation under white LED sources having different spectral characteristics. In addition, a photonic structure of periodically arranged circular dielectric filled holes has been proposed here to enhance conversion efficiency of the PV device when illuminated by the white LED sources. Different shape and arrangement of the holes may improve the optical absorption and charge transport properties of active layers. In terms of more efficient light confinement techniques, multiple photonic patterns (perhaps subdivided between front and back surfaces) can also increase the efficiency compared to a single pattern. This multiple pattern approach can be useful for multi-junction PV cells, where each junction in the stack can be patterned with a photonic lattice whose period has to be tuned depending on the absorption threshold of the active material.

List of References

[1] E. Kabir, P. Kumar, S. Kumar, A. A. Adelodun, and K. Kim, “Solar energy : Potential and future prospects,” *Elsevier*, vol. 82, no. August 2017, pp. 894–900, 2018.

[2] N. Kannan and D. Vakeesan, “Solar energy for future world : - A review,” *Elsevier*, vol. 62, pp. 1092–1105, 2016.

[3] A. Goetzberger, J. Luther, and G. Willeke, “Solar cells : past , present , future,” *Elsevier*, vol. 74, pp. 1–11, 2002.

[4] A. Nasiri, S. Member, S. A. Zabalawi, S. Member, G. Mandic, and S. Member, “Indoor Power Harvesting Using Photovoltaic Cells for Low-Power Applications,” *IEEE Trans. Ind. Electron.*, vol. 56, no. 11, pp. 4502–4509, 2009.

[5] N. H. Reich, W. G. J. H. M. van Sark, and W. C. Turkenburg, “Charge yield potential of indoor-operated solar cells incorporated into Product Integrated Photovoltaic (PIPV),” *Renew. Energy*, vol. 36, no. 2, pp. 642–647, 2011.

[6] M. F. Müller, M. Freunek, and L. M. Reindl, “Maximum efficiencies of indoor photovoltaic devices,” *IEEE J. Photovoltaics*, vol. 3, no. 1, pp. 59–64, 2013.

[7] A. S. Teran *et al.*, “AlGaAs Photovoltaics for Indoor Energy Harvesting in mm-Scale Wireless Sensor Nodes,” *IEEE Trans. Electron Devices*, vol. 62, no. 7, pp. 2170–2175, 2015.

[8] I. Mathews, P. J. King, F. Stafford, and R. Frizzell, “Performance of III-V solar cells as indoor light energy harvesters,” *IEEE J. Photovoltaics*, vol. 6, no. 1, pp. 230–235, 2016.

[9] K. A. Haque and M. Z. Baten, “On the prospect of CZTSSe-based thin film solar cells for indoor photovoltaic applications: A simulation study,” *AIP Adv.*, vol. 9, no. 5, p. 055326, 2019.

[10] A. Virtuani, E. Lotter, and M. Powalla, “Influence of the light source on the low-irradiance performance of Cu(In,Ga)Se2 solar cells,” *Sol. Energy Mater. Sol. Cells*, vol. 90, no. 14, pp. 2141–2149, 2006.

[11] F. De Rossi, T. Pontecorvo, and T. M. Brown, “Characterization of photovoltaic devices for indoor light harvesting and customization of flexible dye solar cells to deliver superior efficiency under artificial lighting,” vol. 156, pp. 413–422, 2015.

[12] M. Freitag *et al.*, “Dye-sensitized solar cells for efficient power generation under ambient lighting,” *Nat. Photonics*, vol. 11, no. 6, pp. 372–378, 2017.

[13] G. Lucarelli, F. Di Giacomo, V. Zardetto, M. Creatore, and T. M. Brown, “Efficient light harvesting from flexible perovskite solar cells under indoor white light-emitting diode illumination,” *Nano Res.*, vol. 10, no. 6, pp. 2130–2145, 2017.

[14] M. Li *et al.*, “Interface Modification by Ionic Liquid: A Promising Candidate for Indoor Light Harvesting and Stability Improvement of Planar Perovskite Solar Cells,” *Adv. Energy Mater.*, vol. 8, no. 24, pp. 1–8, 2018.

[15] A. Bozzola, M. Liscidini, and L. C. Andreani, “Photonic light-trapping versus Lambertian limits in thin film silicon solar cells with 1D and 2D periodic patterns,” *Opt. Soc. Am.*

[16] G. Gomard *et al.*, “Light harvesting by planar photonic crystals in solar cells: The case of amorphous silicon,” *J. Opt.*, vol. 14, no. 2, 2012.

[17] F. Pratesi, M. Burresi, F. Riboli, K. Vynck, and D. S. Wiersma, “Disordered photonic structures for light harvesting in solar cells,” vol. 21, no. May, pp. 460–468, 2013.

[18] K. Ishizaki *et al.*, “Improved efficiency of ultra-thin μc-Si solar cells with photonic-crystal structures,” *Opt. Soc. Am.*, vol. 23, no. 11, pp. 1475–1483, 2015.

[19] D. Duch́, L. Escoubas, J. J. Simon, P. Torchio, W. Vervisch, and F. Flory, “Slow Bloch modes for enhancing the absorption of light in thin films for photovoltaic cells,” *Appl. Phys. Lett.*, vol. 92, no. 19, pp. 1–4, 2008.

[20] A. Mihi, F. J. López-Alcaraz, and H. Míguez, “Full spectrum enhancement of the light harvesting efficiency of dye sensitized solar cells by including colloidal photonic crystal multilayers,” *Appl. Phys. Lett.*, vol. 88, no. 19, 2006.

[21] H. Águas *et al.*, “Thin Film Silicon Photovoltaic Cells on Paper for Flexible Indoor Applications,” *Adv. Funct. Mater.*, vol. 25, no. 23, pp. 3592–3598, 2015.

[22] J. S. Goo, S. C. Shin, Y. J. You, and J. W. Shim, “Polymer surface modification to optimize inverted organic photovoltaic devices under indoor light conditions,” *Sol. Energy Mater. Sol. Cells*, vol. 184, no. January, pp. 31–37, 2018.

[23] C. Y. Chen, J. H. Chang, K. M. Chiang, H. L. Lin, S. Y. Hsiao, and H. W. Lin, “Perovskite Photovoltaics for Dim-Light Applications,” *Adv. Funct. Mater.*, vol. 25, no. 45, pp. 7064–7070, 2015.

[24] H. K. H. Lee *et al.*, “Organic photovoltaic cells-promising indoor light harvesters for self-sustainable electronics,” *J. Mater. Chem. A*, vol. 6, no. 14, pp. 5618–5626, 2018.

[25] B. P. Lechêne, M. Cowell, A. Pierre, J. W. Evans, P. K. Wright, and A. C. Arias, “Organic solar cells and fully printed super-capacitors optimized for indoor light energy harvesting,” *Nano Energy*, vol. 26, pp. 631–640, 2016.

[26] B. Minnaert and P. Veelaert, “Efficiency simulations of thin film chalcogenide photovoltaic cells for different indoor lighting conditions,” *Thin Solid Films*, vol. 519, no. 21, pp. 7537–7540, 2011.

[27] J. Cho, J. H. Park, J. K. Kim, and E. F. Schubert, “White light-emitting diodes: History, progress, and future,” *Laser Photonics Rev.*, vol. 11, no. 2, 2017.

[28] E. F. Schubert and J. K. Kim, “Solid-state light sources getting smart,” *Science (80-.).*, vol. 308, no. 5726, pp. 1274–1278, 2005.

[29] Y. Narukawa *et al.*, “Recent progress of high efficiency white LEDs,” *Phys. Status Solidi Appl. Mater. Sci.*, vol. 204, no. 6, pp. 2087–2093, 2007.

[30] K. Vynck, M. Burresi, F. Riboli, and D. S. Wiersma, “Photon management in two-dimensional disordered media,” *Nat. Mater.*, vol. 11, no. 12, pp. 1017–1022, 2012.

[31] P. Bermel, C. Luo, L. Zeng, L. C. Kimerling, and J. D. Joannopoulos, “Improving thin-film crystalline silicon solar cell efficiencies with photonic crystals,” *Opt. Express*, vol. 15, no. 25, p. 16986, 2007.

[32] D. M. Chapin, C. S. Fuller, and G. L. Pearson, “A new silicon p-n junction photocell for converting solar radiation into electrical power,” *J. Appl. Phys.*, vol. 25, no. 5, pp. 676–677, 1954.

[33] E. Spooner, “Organic Photovoltaics vs. 2nd-Generation Solar Cell Technologies.”

[34] A. Goetzberger, J. Luther, and G. Willeke, “Solar cells : past , present , future,” vol. 74, pp. 1–11, 2002.

[35] J. Lee, B. Bagheri, and H. A. Kao, “A Cyber-Physical Systems architecture for Industry 4.0-based manufacturing systems,” *Manuf. Lett.*, vol. 3, pp. 18–23, 2015.

[36] A. Tzounis, N. Katsoulas, T. Bartzanas, and C. Kittas, “Internet of Things in agriculture, recent advances and future challenges,” *Biosyst. Eng.*, vol. 164, pp. 31–48, 2017.

[37] H. Fang, J. Liu, Z. Xu, L. Dong, L. Wang, and D. Chen, “Fabrication and

performance of MEMS-based piezoelectric power generator for vibration energy harvesting," *Microelectronics J.*, vol. 37, pp. 1280–1284, 2006.

[38] D. Bouchouicha, F. Dupont, M. Latrach, and L. Ventura, "Ambient RF Energy Harvesting Abstract :," pp. 2–6, 2010.

[39] J. P. Carmo, L. M. Gonçalves, and J. H. Correia, "Thermoelectric Microconverter for Energy Harvesting Systems," *IEEE Trans. Ind. Electron.*, vol. 57, no. 3, pp. 861–867, 2010.

[40] H. Yu, "Power Management and Energy Harvesting for Indoor Photovoltaic Cells System," in *2011 Second International Conference on Mechanic Automation and Control Engineering*, 2011, pp. 521–524.

[41] I. Mathews, S. N. Kantareddy, T. Buonassisi, and I. M. Peters, "Technology and Market Perspective for Indoor Photovoltaic Cells," *Joule*, vol. 3, no. 6, pp. 1415–1426, 2019.

[42] M. Thesis, "Two-Dimensional Drift-Di usion Simulation of Organic Solar Cells," no. February, 2016.

[43] B. Padmanabhan, "MODELING OF SOLAR CELLS," 2008.

[44] S. D. Gedney, *Introduction to the Finite-Difference Time-Domain (FDTD)) method for electromagnetics*, vol. 27. 2011.

[45] K. S. YEE, "Numerical Solution of Initial Boundary Value Problems Involving Maxwell's Equations in Isotropic Media," vol. 21, pp. 302–307, 1966.

[46] B. Lord, "On Reflection of Vibrations . Professor of Experimental Physics in the University of Lord Rayleigh on," *Ann. Phys.*, pp. 51–56, 1880.

[47] Y. C. Chao, C. Y. Chen, C. A. Lin, and J. H. He, "Light scattering by nanostructured anti-reflection coatings," *Energy Environ. Sci.*, vol. 4, no. 9, pp. 3436–3441, 2011.

[48] C. Rockstuhl *et al.*, "Randomly Textured Surfaces," *Phot. Manag. Sol. Cells*, pp. 91–116, 2015.

[49] E. YABLONOVITCH and G. D. CODY, "Intensity Enhancement in Textured Optical Sheets for Solar Cells," *IEEE Trans. Electron Devices*, vol. 33, no. 11, pp. 1834–1835, 1986.

[50] C. Rockstuhl *et al.*, "Comparison and optimization of randomly textured surfaces in thin-film solar cells," *Opt. Express*, vol. 18, no. S3, p. A335, 2010.

[51] M. Peters *et al.*, “Rear Side Diffractive Gratings for Silicon Wafer Solar Cells,” *Phot. Manag. Sol. Cells*, pp. 49–90, 2015.

[52] M. Wellenzohn and R. Hainberger, “Light trapping by backside diffraction gratings in silicon solar cells revisited,” *Opt. Express*, vol. 20, no. S1, p. A20, 2012.

[53] J. Gjessing, A. Sudbø, and E. S. Marstein, “2D blazed grating for light trapping in thin silicon solar cells,” *Opt. InfoBase Conf. Pap.*, vol. 18, no. 6, pp. 5481–5495, 2010.

[54] X. Meng, E. Drouard, G. Gomard, R. Peretti, A. Fave, and C. Seassal, “Combined front and back diffraction gratings for broad band light trapping in thin film solar cell,” *Opt. Express*, vol. 20, no. S5, p. A560, 2012.

[55] A. R. Knapitsch, “Photonic Crystals: Enhancing the Light Output of Scintillation Based Detectors,” 2012.

[56] G. Von Plessen, D. Kumar, F. Hallermann, D. N. Chigrin, and A. N. Sprafke, “Linear Optics of Plasmonic Concepts to Enhance Solar Cell Performance,” *Phot. Manag. Sol. Cells*, pp. 209–230, 2015.

[57] H. A. Atwater1 and A. Polman2, “Plasmonics for improved photovoltaic devices,” *Nat. Mater.*, vol. 2, no. 6, pp. 402–407, 2003.

[58] K. L. Kelly, E. Coronado, L. L. Zhao, and G. C. Schatz, “The optical properties of metal nanoparticles: The influence of size, shape, and dielectric environment,” *J. Phys. Chem. B*, vol. 107, no. 3, pp. 668–677, 2003.

[59] K. R. Catchpole and A. Polman, “Plasmonic solar cells,” *Opt. Express*, vol. 16, no. 26, p. 21793, 2008.

[60] P. Vijayakumar, “CCT AND CRI IN LED LIGHTING -AN58765 CCT and CRI in LED Lighting,” 2013.

[61] “LSPDD: Lamp Spectral Power Distribution Database.” [Online]. Available: http://galileo.graphycs.cegepsherbrooke.qc.ca/app/en/home.

[62] M. S. Shur and A. Žukauskas, “Solid-state lighting: Toward superior illumination,” *Proc. IEEE*, vol. 93, no. 10, pp. 1691–1703, 2005.

[63] W. Wang *et al.*, “Device characteristics of CZTSSe thin-film solar cells with 12.6% efficiency,” *Adv. Energy Mater.*, vol. 4, no. 7, pp. 1–5, 2014.

[64] N. Amin, T. Isaka, A. Yamada, and M. Konagai, “Highly efficient 1 μm thick

CdTe solar cells with textured TCOs," *Sol. Energy Mater. Sol. Cells*, vol. 67, no. 1–4, pp. 195–201, 2001.

[65] M. P. Paranthaman, W. Wong-Ng, and R. N. Bhattacharya, "Preface," in *Semiconductor Materials for Solar Photovoltaic Cells*, vol. 4, 2015, pp. v–viii.

[66] A. Morales-Acevedo, "Thin film CdS/CdTe solar cells: Research perspectives," *Sol. Energy*, vol. 80, no. 6, pp. 675–681, 2006.

[67] K. Jacobi, G. Zwicker, and A. Gutmann, "Work function, electron affinity and band bending of zinc oxide surfaces," *Surf. Sci.*, vol. 141, no. 1, pp. 109–125, 1984.

[68] D. S. M. E. OZSAN, D. R. JOHNSON, M. SADEGHI, "Optical and electrical characterization of CdS thin films," *J. Mater. Sci. Mater. Electron.*, vol. 54, no. 7, pp. 119–125, 1996.

[69] J. He *et al.*, "Single-step preparation and characterization of Cu 2ZnSn(S xSe 1-x) 4 thin films deposited by pulsed laser deposition method," *J. Alloys Compd.*, vol. 529, pp. 34–37, 2012.

[70] J. Robertson and S. J. Clark, "Limits to doping in oxides," *Phys. Rev. B - Condens. Matter Mater. Phys.*, vol. 83, no. 7, pp. 1–7, 2011.

[71] T. Gokmen, O. Gunawan, and D. B. Mitzi, "Semi-empirical device model for Cu2ZnSn(S,Se)4 solar cells," *Appl. Phys. Lett.*, vol. 105, no. 3, pp. 2–7, 2014.

[72] X. Yang, C. Xu, and N. C. Giles, "Intrinsic electron mobilities in CdSe, CdS, ZnO, and ZnS and their use in analysis of temperature-dependent Hall measurements," *J. Appl. Phys.*, vol. 104, no. 7, 2008.

[73] D. H. Kuo and M. Tsega, "Hole mobility enhancement of Cu-deficient Cu1.75Zn(Sn 1-xAlx)Se4 bulks," *J. Solid State Chem.*, vol. 206, pp. 134–138, 2013.

[74] K. Durose, P. R. Edwards, and D. P. Halliday, "Materials aspects of CdTe/CdS solar cells," *J. Cryst. Growth*, vol. 197, no. 3, pp. 733–742, 1999.

[75] L. Kranz *et al.*, "Doping of polycrystalline CdTe for high-efficiency solar cells on flexible metal foil," *Nat. Commun.*, vol. 4, 2013.

[76] P. W. Davis and T. S. Shilliday, "Some optical properties of cadmium telluride," *Phys. Rev.*, vol. 118, no. 4, pp. 1020–1022, 1960.

[77] A. Kanevce and T. A. Gessert, "Optimizing CdTe solar cell performance: Impact

of variations in minority-carrier lifetime and carrier density profile," *IEEE J. Photovoltaics*, vol. 1, no. 1, pp. 99–103, 2011.

[78] "Refractive Index Database." [Online]. Available: https://refractiveindex.info/.

[79] Janos Schanda, Ed., "CIE Colorimetry," in *Colorimetry: Understanding the CIE System*, John Wiley & Sons, pp. 27–35.

[80] C. S. McCamy, "Correlated color temperature as an explicit function of chromaticity coordinates," *Color Res. Appl.*, vol. 17, no. 2, pp. 142–144, 1992.

[81] N. Amin, K. Sopian, and M. Konagai, "Numerical modeling of CdS/CdTe and CdS/CdTe/ZnTe solar cells as a function of CdTe thickness," *Sol. Energy Mater. Sol. Cells*, vol. 91, no. 13, pp. 1202–1208, 2007.

[82] A. Gupta, V. Parikh, and A. D. Compaan, "High efficiency ultra-thin sputtered CdTe solar cells," *Sol. Energy Mater. Sol. Cells*, vol. 90, no. 15, pp. 2263–2271, 2006.

[83] P. Examiner and V. Afremova, "HIGH EFFICIENCY LEDS AND LED LAMPS," 1995.

[84] A. A. Setlur *et al.*, "Energy-efficient, high-color-rendering LED lamps using oxyfluoride and fluoride phosphors," *Chem. Mater.*, vol. 22, no. 13, pp. 4076–4082, 2010.

[85] W. Wang *et al.*, "Device characteristics of CZTSSe thin-film solar cells with 12.6% efficiency," *Adv. Energy Mater.*, 2013.

[86] "First Solar Hits Record 22.1% Conversion Efficiency for CdTe Solar Cell," 23-Feb-2016.

[87] X. Meng *et al.*, "Absorbing photonic crystals for silicon thin-film solar cells : Design , fabrication and experimental investigation," *Sol. Energy Mater. Sol. Cells*, vol. 95, pp. S32–S38, 2011.

[88] N. D. Gupta, V. Janyani, and S. M. Ieee, "Design and Analysis of Light Trapping in Thin Film GaAs Solar Cells using 2D Photonic Crystal Structures at front surface," vol. 9197, no. c, 2017.